

# A Regionally Adaptable Ground-Motion Model for Fourier Amplitude Spectra of Shallow Crustal Earthquakes in Europe

Sreeram Reddy Kotha (✉ [sreeram-reddy.kotha@univ-grenoble-alpes.fr](mailto:sreeram-reddy.kotha@univ-grenoble-alpes.fr))

Institut des Sciences de la Terre <https://orcid.org/0000-0002-4874-3730>

Dino Bindi

Helmholtz-Zentrum Potsdam GFZ: Deutsches Geoforschungszentrum Potsdam

Fabrice Cotton

University of Potsdam: Universitat Potsdam

---

## Research Article

**Keywords:** Ground-motion model, Fourier spectra, robust mixed-effects regression, regionally adaptable, seismic hazard and risk, Europe

**Posted Date:** April 15th, 2021

**DOI:** <https://doi.org/10.21203/rs.3.rs-377090/v1>

**License:**  This work is licensed under a Creative Commons Attribution 4.0 International License.

[Read Full License](#)

---

**Version of Record:** A version of this preprint was published at Bulletin of Earthquake Engineering on October 30th, 2021. See the published version at <https://doi.org/10.1007/s10518-021-01255-1>.

# A Regionally Adaptable Ground-Motion Model for Fourier Amplitude Spectra of Shallow Crustal Earthquakes in Europe

Sreeram Reddy Kotha<sup>1, 2</sup>, Dino Bindi<sup>2</sup>, Fabrice Cotton<sup>2, 3</sup>

## Abstract

Typical ground-motion models predict the response spectral ordinates (GMM-SA), which are the damped responses of a suite of single-degree-of-freedom oscillators. Response spectra represent the response of an idealized structure to input ground-motion, but not the physics of the actual ground-motion. To complement the regionally adaptable GMM-SA of Kotha et al. (2020), we introduce here a model capable of predicting Fourier amplitudes (GMM-FA); developed from the same Engineering Strong Motion (ESM) dataset for pan-Europe. This GMM-FA reveals the very high variability of high frequency ground-motions, which are completely masked in a GMM-SA. By maintaining the development strategies of GMM-FA identical to that of the GMM-SA, we are able to evaluate the physical meaning of the spatial variability of anelastic attenuation and source characteristics. We find that a fully data-driven geospatial index, Activity Index (AIX), correlates well with the spatial variability of these physical effects. AIX is a fuzzy combination of seismicity and crustal parameters, and can be used to adapt the attenuation and source non-ergodicity of the GMM-FA to regions and tectonic localities sparsely sampled in ESM. While AIX, and a few other parameters we touch upon, may help understand the spatial variability of high frequency attenuation and source effects, the high frequency site-response variability - dominating the overall aleatory variance - is yet unresolvable. With the rapid increase in quantity and quality of ground-motion datasets, we call for an upgrade of regionalization techniques, site-characterisation, and a paradigm shift to Fourier ground-motion models to complement the traditional response spectra prediction models.

*Keywords:* Ground-motion model, Fourier spectra, robust mixed-effects regression, regionally adaptable, seismic hazard and risk, Europe

---

Sreeram Reddy Kotha

[sreeram-reddy.kotha@univ-grenoble-alpes.fr](mailto:sreeram-reddy.kotha@univ-grenoble-alpes.fr)

<https://orcid.org/0000-0002-4874-3730>

<sup>1</sup> Univ. Grenoble Alpes, Univ. Savoie Mont Blanc, CNRS, IRD, IFSTTAR, ISTERre, 38000 Grenoble, France

<sup>2</sup> Helmholtz Centre Potsdam, GFZ German Research Centre for Geosciences, 14467 Potsdam, Germany

<sup>3</sup> University of Potsdam, Institute of Geosciences, Potsdam, Germany

# 1 INTRODUCTION

Typical ground-motion models (GMMs) used in seismic hazard and risk assessments predict the random distribution of ground-motion in terms of spectral amplitude ( $SA$ ), i.e. damped response of an elastic single-degree-of-freedom (SDOF) oscillator with fundamental resonance period  $T$ . In Kotha et al. (2020) we introduced the regionally adaptable GMM derived from the Engineering Strong-Motion (ESM) dataset (Bindi et al. 2019a; Lanzano et al. 2018), developed specifically to predict the 5% damped response spectra  $SA(T)$  of shallow crustal earthquakes in Europe and Mediterranean regions (GMM-SA from hereon). GMM-SAs are quite useful in engineering applications because they predict the response of idealized SDOF structures to input ground-motion. However,  $SA(T)$  integrate characteristics of Fourier amplitudes over a range of frequencies  $FA(f)$ , and hence do not exactly represent the actual ground-motion itself. Therefore, a GMM capable of predicting the actual ground-motion  $FA(f)$  (GMM-FA from hereon) can be a useful alternative to GMM-SA (Bora et al. 2014).

Recollecting from Bayless and Abrahamson (2019b), there are several advantages of GMM-FA over GMM-SA: (1) behavior of a GMM-FA is easier to constrain using seismological theory and models such as Brune (1970) and Boore et al. (2014a); (2) linear site-response remains linear at all frequencies and does not depend on the spectral content of input motions, which isn't the case with  $SA(T)$  according to Bora et al. (2016); (3) calibration of input parameters and methods for finite-fault simulations is more appropriate using GMM-FAs than using GMM-SAs; and (4) inter-frequency correlation of  $FA(f)$ , developed from residuals of a GMM-FA, can facilitate stochastic simulation of realistic ground-motions (Bayless and Abrahamson 2019a; Stafford 2017). In addition, using the random vibration theory (RVT) framework of Bora et al. (2016) one can conveniently generate  $SA(T)$  from a GMM-FA.

Alongside the GMM-SA of Kotha et al. (2020), the ESM dataset provides also an opportunity to develop a GMM-FA for shallow crustal earthquakes originating in the pan-European region; extending from Pyrenness in the west to North-Eastern Anatolian fault system of Turkey. As it is, there are very few GMM-FA developed for this region – the most recent one being that of Bora et al. (2014) derived from an older pan-European strong ground-motion dataset RESORCE (Akkar et al. 2014). Bindi et al. (2019a) developed a GMM-FA from the ESM dataset, but it was not intended for engineering application but to perform a sanity check of data through residual analysis. Essentially, the last update of a compendium of GMMs published since 1964 by Douglas (2011) features only 18 models that predict Fourier Amplitude Spectra (FAS). Therefore, given their practical relevance, we consider it is worth introducing a new GMM-FA to better explore the FAS ground-motion prediction epistemic uncertainty.

Our intention for this new GMM-FA is in fact more than to contribute to the list of usable models. We proposed a regionally adaptable GMM-SA in Kotha et al. (2020), whose partially non-ergodic median predictions [of  $SA(T)$ ] can be adjusted using the various attenuating region, tectonic locality, and site-specific random-effects. The statistical significance of random-effect groups and

1 overall improvement in GMM-SA performance has already been demonstrated in that paper. However,  
 2 what remained unevaluated was the physical meaning of these random-effects, and their adaptability to  
 3 regions with no data in ESM. Correlating the GMM-SA random-effects estimated in response spectral  
 4 domain to geophysical, geological indices did not seem appropriate. For instance, the short-period SAs  
 5 integrate features of moderate-high frequency *FAS*, making it difficult to interpret physically the  
 6 quantified random-effects at  $T < 0.5s$ . Towards this end, in this study we introduce a regionally  
 7 adaptable GMM-FA, correlate the regional adjustments to an independently derived geospatial index,  
 8 and suggest using these correlation to adapt the model to regions with little to no data in the ESM dataset.

9 Our best candidate geospatial index is the Activity Index developed by Chen et al. (2018).  
 10 Although we have tried a suite of geological and geophysical parameters (e.g. Moho depth, 1Hz coda Q  
 11 maps, etc) to serve as proxy for our regional adjustments (the random-effects), the spatial coverage and  
 12 resolution, and the epistemic uncertainty of these parameters made them less viable than the globally  
 13 available Activity Index. More about this parameter will be discussed in relevant sections.

## 14 2 GROUND-MOTION DATASET

15 The ground-motion dataset we used is the Fourier amplitude version of the ESM dataset. The Fourier  
 16 version of ESM does not contain data from Iran, and is therefore a few dozen records smaller than that  
 17 used to derive the Kotha et al. (2020) GMM-SA. The ground-motion data selection criteria,  
 18 regionalisation models, functional form, and regression methods are identical to that of the Kotha et al.  
 19 (2020) GMM-SA - except for a few minor changes noted subsequently:

- 20 1) We select only those events classified as non-subduction events by Weatherill et al. (2020d). The  
 21 selection removes in-slab, interface, outer-rise, and upper-mantle events from the regression dataset.  
 22 The resulting 923 events with hypocentral depth  $0 < D \leq 39km$  are located in regions with  $14 \leq$   
 23 *Moho depth*  $\leq 49km$ , as per the Moho map of Grad et al. (2009). Note that the same selection  
 24 criteria resulted in 927 events in case of GMM-SA
- 25 2) Only those events with  $\geq 3$  records in the dataset are used in regression. Also, wherever available,  
 26 the harmonised  $M_W$  estimates according to the European Mediterranean Earthquake Catalogue  
 27 [EMEC] (Grünthal and Wahlström 2012) are preferred over the ESM default values. As with GMM-  
 28 SA, preference of EMEC  $M_W$  is to maintain consistency with the seismic source models developed  
 29 for the new European Seismic Hazard Map (ESHM20)
- 30 3) We keep data from all 1622 sites in the dataset irrespective of whether their  $V_{S30}$  measured from  
 31 geotechnical investigations is provided or not in ESM. This is to estimate the site-specific terms  
 32 ( $\delta S_2 S_5$ ) at as many sites as possible, and then explore various site-response proxies to characterize  
 33 them (Kotha et al. 2018; Weatherill et al. 2020b). Note that the GMM-SA used data from 1829 sites,  
 34 including 197 sites from Iran whose data is unavailable in the Fourier version of ESM

- 1 4) Choice of distance metric is  $R_{JB}$  where available, otherwise the epicentral distance  $R_{epi}$  – but only  
 2 for events with  $M_W \leq 6.2$ . The distance range is not truncated and extends up to  $R_{JB} = 477km$ . In  
 3 comparison, the GMM-SA was derived from data extending up to  $R_{JB} = 545km$
- 4 5) The only additional record selection criterion relevant to the GMM-FA is the low-pass frequency  
 5 filter limit. For the GMM-SA regression of  $SA(T)$ , we chose only the records with a high-pass filter  
 6 frequency of both horizontal components  $f_{hp} \leq 0.8/T$ . While for the GMM-FA regression  
 7 of  $FA(f)$ , we chose the records with high-pass frequency  $f_{hp} \leq 0.8f$  and low-pass frequency  $f_{lp} \geq$   
 8  $f/0.8$ , of both horizontal components.
- 9 6) The GMM-FA is developed to predict the Effective Amplitude Spectra [EAS as defined by Pacific  
 10 Earthquake Engineering Research Centre (Goulet et al. 2018)] of the two horizontal  $FA(f)$   
 11 components, for 25 values of  $f$  in the range  $0.15Hz - 20Hz$ . EAS is an orientation independent  
 12 horizontal-component  $FA(f)$  of ground-motion that can be used with RVT framework to estimate  
 13  $SA(T)$  (Bora et al. 2019)

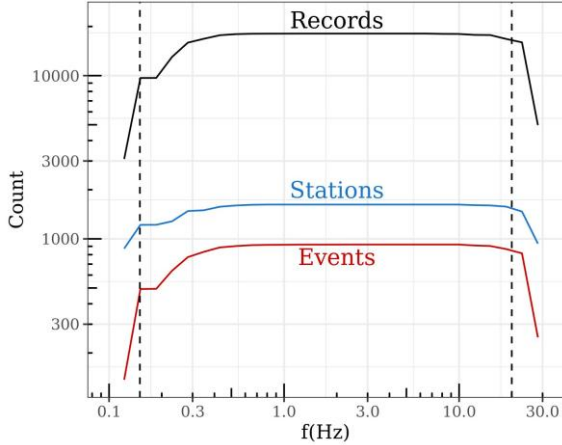


**Fig.1** Number of records, events, and stations used in regression at each frequency

14  
 15 Following the above criteria, the number of records from  $3.1 \leq M_W \leq 7.4$  events at distances  
 16  $0 \leq R_{JB} < 477km$  available for GMM-FA regression is shown in Fig.1

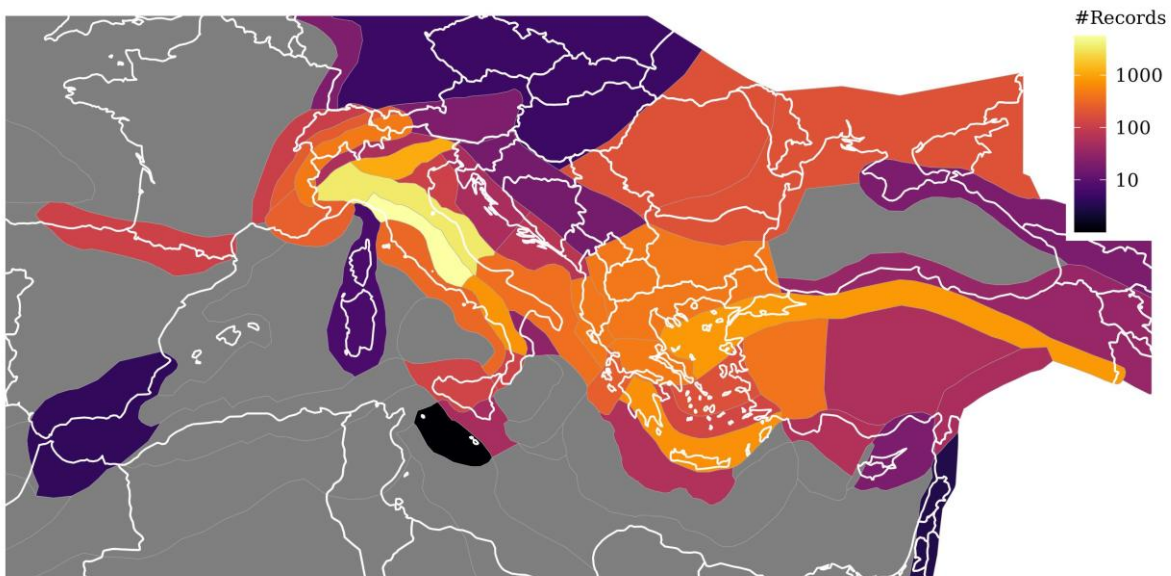
### 17 3 REGIONALISATION DATASETS

18 The GMM-SA of Kotha et al. (2020) is a regionally adaptable model, wherein the event and path effects  
 19 are regionalised. It is capable of predicting  $SA(T)$  accounting the regional differences in distance decay  
 20 through  $\Delta c_{3,r}(T) \approx \mathcal{N}(0, \tau_{c3}(T))$  and average of localised source effects through  $\Delta L2L_l(T) \approx$   
 21  $\mathcal{N}(0, \tau_{L2L}(T))$ , and site-specific effects through  $\Delta S2S_s(T) \approx \mathcal{N}(0, \phi_{s2s}(T))$  random-effect  
 22 adjustments to the generic GMM-SA median ( $\ln(\mu)$ ). We use the same regionalisation models for  
 23 GMM-FA, and therefore, regionalise the data identically. Regional differences in locality-specific event  
 24 and region-specific anelastic attenuation characteristics are estimated as random-effects in a mixed-  
 25 effects regression. The GMM-FA random-effect values can be used in three ways: 1) in region- and  
 26 locality-specific predictions accounting their epistemic uncertainties, 2) ignored while reintroducing

1 their random-variances into total aleatoric variability of ergodic GMM-FA predictions – i.e. no region-  
 2 and locality-specific adaption, 3) investigated for correlation with geophysical parameters or proxies in  
 3 order to extend their usage to regions with no data in ESM. Kotha et al. (2020) demonstrated the first  
 4 two applications, while also evaluating the robustness of region- and locality-specific GMM-SA through  
 5 a 10-fold cross validation exercise. In this study we discuss the third approach, i.e. evaluating the  
 6 physical meaning and adaptability of the GMM-FA random-effects.

### 7 3.1 ATTENUATION REGIONALISATION

8 In a drive towards regionalising ground-motion predictions, a few recent GMM-SAs identified and  
 9 quantified between-region variability of anelastic attenuation, and attributed it to spatial variability of  
 10 crustal characteristics. These GMM-SAs were regionalised based on geopolitical boundaries, in absence  
 11 of a more relevant geophysical regionalisation. However, spatial variability of attenuation captured by  
 12 the 1 Hz coda Q maps of smaller regions within geopolitical boundaries is quite high; as shown for Italy  
 13 and Turkey by Cong and Mitchell (1998), for mainland France by Mayor et al. (2018), and for Europe  
 14 in general by Pilz et al. (2019).



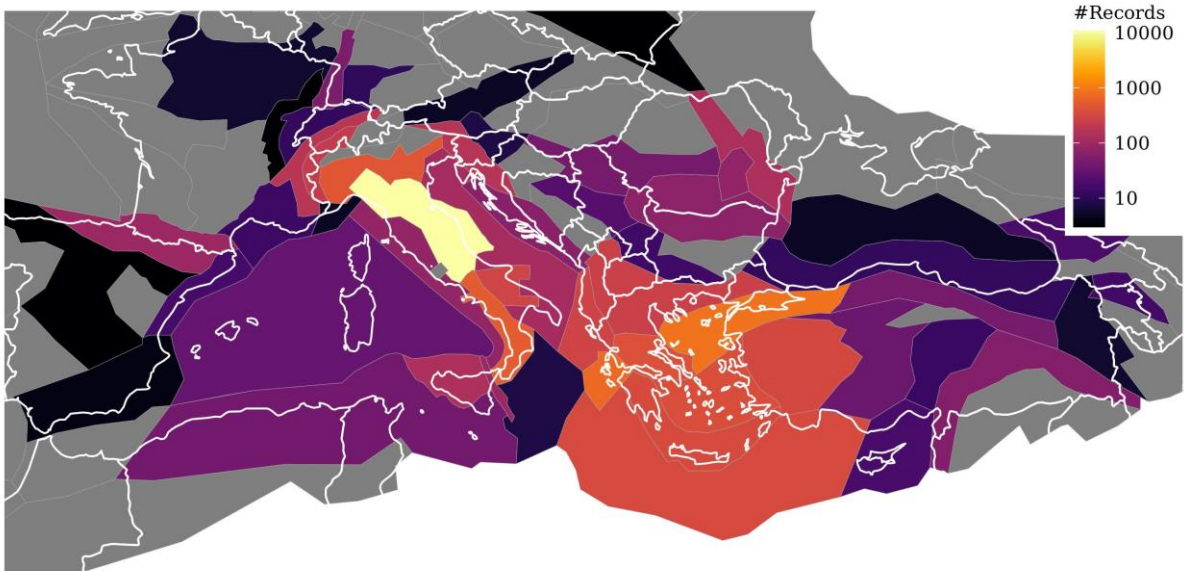
15 **Fig.2** Distribution of records in each of the 45 attenuation regionalisation polygons

16 In this study, as in Kotha et al. (2020), we chose instead of geopolitical boundaries, a geological-  
 17 geophysical regionalisation model developed by Basili et al. (2019) in the TSUMAPS-NEAM project.  
 18 Fig.2 shows the TSUMAPS-NEAM regionalisation and the number of records in each attenuating  
 19 region, as determined by the location of the recording sites. Assuming that anelastic attenuation is a  
 20 dominant phenomenon at far-source distances (e.g.  $R_{JB} \geq 80km$ ) and in near-surface crustal layers, we  
 21 let the location of the receiving site decide to which attenuating region a particular ground-motion record  
 22 should be allotted to.

1 The 45 regions in this map (Fig.2) divide Turkey into around eight distinct attenuating regions,  
 2 East and West Anatolia being the largest, while Italy is divided into 12 regions. Fig.2 also shows that  
 3 while some regions have a few thousand records assigned (e.g. the central and northern Apennines), there are few  
 4 regions with only a few dozen records (e.g. only 13 in the Rhine Graben). In mixed-effects regression  
 5 terminology, the random-variance of the *group* of attenuation regions quantifies the observed variability  
 6 of anelastic attenuation between regions, where regions are *levels* of the group. If the random variance  
 7 of this group is non-zero, it means that the chosen regionalisation scheme is able to capture the spatial  
 8 variability of anelastic attenuation. Complementing the Kotha et al. (2020), in this study, we evaluate  
 9 physical meaning of the region-specific random-effects.

### 10 3.2 EVENT LOCALISATION

11 Alongside the traditional earthquake-to-earthquake variability captured by the between-event random-  
 12 effect group  $\Delta B_e \approx \mathcal{N}(0, \tau_e)$ , Kotha et al. (2020) introduced an additional random-effect to quantify  
 13 locality-to-locality variability of earthquake characteristics; analogues to the location-to-location  
 14 variability  $\Delta L2L_l \approx \mathcal{N}(0, \tau_{L2L})$ , of Al Atik et al. (2010). We assign the 923 shallow crustal events in  
 15 the ESM dataset to 55 seismotectonic zones defined in the European Seismic Hazard Model 2020  
 16 (ESHM20). The seismotectonic source zonation (called "TECTO") was designed to distinguish regional  
 17 tectonic features influencing the generation of crustal earthquakes, but not the very localised features.  
 18 'TECTO' was thus a good model for earthquake source localisation in Kotha et al. (2020), and distinct  
 19 from the TSUMAPS-NEAM of Basili et al. (2019) used for regionalisation of anelastic attenuation.



20 **Fig.3** Distribution of records from shallow crustal events in each of the 55 event localisation polygons (tectonic zones)

21 As in Kotha et al. (2020), this random-effects group is the between- locality  $\Delta L2L_l \approx$   
 22  $\mathcal{N}(0, \tau_{L2L})$ , wherein the levels are tectonic localities (locality  $l$ ) containing their assigned ESM crustal

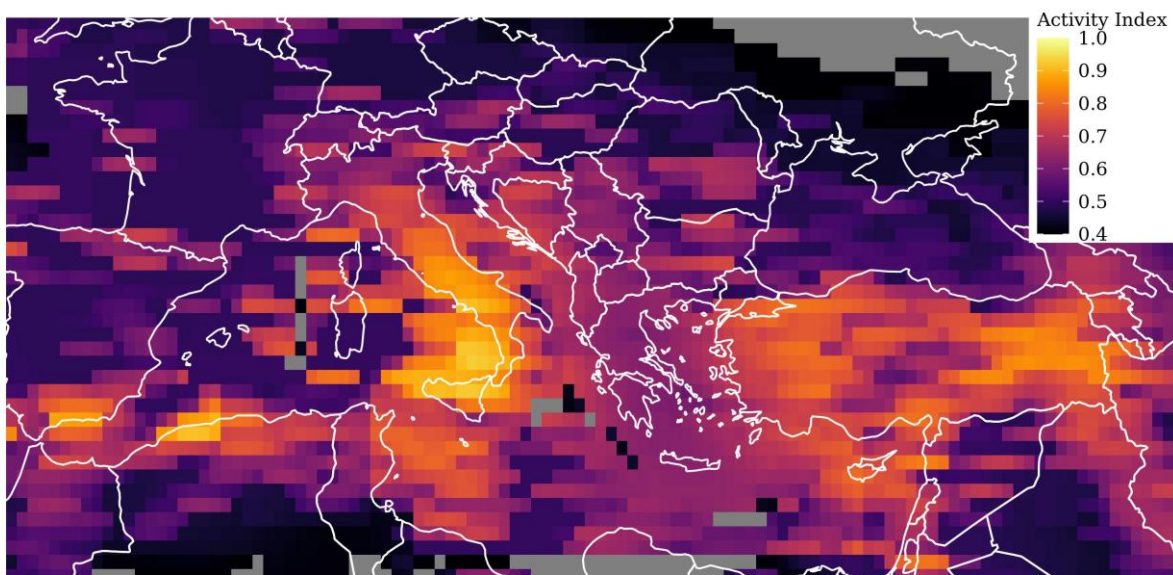
1 events and records. Fig.3 shows the distribution of records from active shallow crustal events within the  
 2 event localisation polygons. As with the attenuating region group, this group is introduced to quantify  
 3 the earthquake locality-to-locality variability of ground-motion in the dataset through the between-  
 4 locality variance ( $\tau_{L2L}^2$ ), which if zero indicates that the regionalisation model is not able to identify any  
 5 significant spatial variability of earthquake characteristics.

### 6 3.3 ACTIVITY INDEX

7 Chen et al. (2018) introduced a fully data-driven global tectonic regionalisation model for selection of  
 8 ground-motion models in seismic hazard applications. Based on a fuzzy logic workflow, they have  
 9 rendered a regular grid with a spacing of  $0.5^\circ$ , wherein each cell is assigned a probability of being an  
 10 active tectonic region – the Activity Index (AIx), as shown in Fig.4. AIx in a grid cell is calculated from  
 11 the following fuzzy rules:

- 12 1) **High AIx** – IF [seismic moment rate density] is ‘High’, AND [1Hz Lg coda Q] is ‘Low’, AND [S-  
 13 wave velocity variation at 175km] is ‘Low’, THEN the region is [‘Active’]
- 14 2) **Low AIx** – IF [seismic moment rate density] is ‘Low’, AND [1Hz Lg coda Q] is ‘High’ AND [S-  
 15 wave velocity variation at 175km] is ‘High’, THEN the region is [‘Stable’]

16 AIx is derived as a of combination of seismic moment rate density (Weatherill et al. 2016), 1Hz  
 17 Lg coda Q (Mitchell et al. 2008), and shear-wave velocity variation at 175km (Ritsema et al. 2011). We  
 18 use this dataset to evaluate the various regional variabilities quantified as the GMM random-effects.



19 **Fig.4** Activity Index map of pan-European region by Chen et al. (2018)

## 20 4 FUNCTIONAL FORM

21 A mixed-effects GMM is composed of fixed-effects and random-effects. Fixed-effects part of the GMM  
 22 is the continuous function built as a combination of predictor variables, which in this case are event

1 magnitude  $M_W$  and event-to-site distance metric  $R_{JB}$  (in km). As suggested by Fukushima (1996), and  
 2 later in Bora et al. (2017) and Bora et al. (2019), the fixed-effects component of our GMM-FA remains  
 3 the same as GMM-SA presented in Kotha et al. (2020). However, although recent GMM-FA models  
 4 from NGA-West2 dataset (Ancheta et al. 2014) by Bayless and Abrahamson (2019b) and Bora et al.  
 5 (2019) retained a magnitude-dependent geometrical spreading component, following the suggestion by  
 6 Cotton et al. (2008) we have dropped this term from our GMM-FA; which in the Kotha et al. (2020)  
 7 GMM-SA was the coefficient  $c_2$ .

$$\ln(\mu) = e_1 + f_{R,g}(M_W, R_{JB}) + f_{R,a}(R_{JB}) + f_M(M_W) + \delta L2L_l + \delta B_{e,l}^0 + \delta S2S_s + \varepsilon \quad (1)$$

$$f_{R,g} = c_1 \cdot \ln^2 \sqrt{(R_{JB}^2 + h_D^2)/(R_{ref}^2 + h_D^2)} \quad (2)$$

$$f_{R,a} = \frac{c_3}{100} \cdot (\sqrt{R_{JB}^2 + h_D^2} - \sqrt{R_{ref}^2 + h_D^2}) \quad (3)$$

$$f_M = \begin{cases} b_1 \cdot (M_W - M_h) + b_2 \cdot (M_W - M_h)^2 & M_W \leq M_h \\ b_3 \cdot (M_W - M_h) & M_h < M_W \end{cases} \quad (4)$$

8 In the mixed-effects formulation of equation (1),  $f_{R,g}$ ,  $f_{R,a}$ ,  $f_M$  are the fixed-effects components;  
 9 wherein  $e_1$ ,  $b_1$ ,  $b_2$ ,  $b_3$ ,  $c_1$ ,  $c_3$  are the fixed-effects regression coefficients (eq. 2 and 3). Regarding the  
 10 random-effects components:

- 11 1) Between-region random-effects follow a Gaussian distribution  $\Delta c_{3,r} = \mathcal{N}(0, \tau_{c3})$ .  $\tau_{c3}$  quantifies  
 12 the between-region variability of anelastic attenuations across the attenuating regions  $r$  introduced  
 13 earlier in Fig.2. Alongside a generic region-independent  $c_3$ , region-specific adjustments  $\delta c_{3,r}$  are  
 14 estimated as random-effects for the 45 attenuation regions. For region-specific GMM-FA  
 15 predictions we replace the apparent anelastic attenuation term  $c_3$  in equation (3) with a  $c_{3,r} = c_3 +$   
 16  $\delta c_{3,r}$
- 17 2) Between-locality variability of observed ground-motions are captured by the random-effect  
 18  $\Delta L2L = \mathcal{N}(0, \tau_{L2L})$ . Locality-specific adjustments  $\delta L2L_l$ , estimated for the 55 localities  $l$  shown in  
 19 Fig.3, can be used to make locality-specific ground-motion predictions by replacing the offset  $e_1$  in  
 20 equation (1) with  $e_{1,l} = e_1 + \delta L2L_l$
- 21 3) Event-to-event variability in this GMM is the *traditional* between-event random-effects  $\Delta B_e =$   
 22  $\mathcal{N}(0, \tau_e)$  filtered for between-locality variability  $\Delta L2L_l = \mathcal{N}(0, \tau_{L2L})$ , and is now captured by  
 23 the  $\Delta B_{e,l}^0 = \mathcal{N}(0, \tau_0)$ ; where, for an event  $e$  located in tectonic locality  $l$ , the event-specific term

1 can be seen as  $\delta B_{e,l}^0 \approx \delta B_e - \delta L2L_l$ .  $\tau_0$  is the generic event-to-event variability corrected for  
 2 locality-to-locality variability, and does not vary with locality  $l$

- 3 4) Site-to-site response variability is captured by the site-specific random-effects  $\Delta S2S = N(0, \phi_{S2S})$ .  
 4 The potential of  $\delta S2S_s$  in site-specific GMM-SAs is well-known, and are useful in studying  
 5 regional differences in site-response scaling with  $V_{S30}$  (time-averaged shear-wave velocity in 30m  
 6 top-soil) as in Kotha et al. (2016), topographic slope and geology as in Weatherill et al. (2020a) or  
 7 a variety of site parameters (Kotha et al. 2018; Pilz and Cotton 2019; Zhu et al. 2020), and even in  
 8 site-specific seismic risk assessment (Kohrangi et al. 2020). Site-specific GMM-FA adjustments  
 9  $\delta S2S_s$ , estimated for the 1622 sites  $s$  in the dataset Fig.3, can be used to make site-specific ground-  
 10 motion predictions by replacing the offset  $e_1$  in equation (1) with  $e_{1,s} = e_1 + \delta S2S_s$
- 11 5) The left-over residuals  $\varepsilon = N(0, \phi)$  contain the unexplained natural variability of ground-motion  
 12 observations, and thus represent the apparent aleatory variability of the model. These residuals can  
 13 be investigated for less dominant phenomenon, such as the anisotropic shear-wave radiation pattern  
 14 at near-source distances (Kotha et al. 2019), anelastic attenuation effects in far-source distances  
 15 (Sahakian et al. 2019), non-linear soil response (Loviknes et al. 2021), etc.

16 In all, this GMM has four random-effect groups. With this configuration of mixed-effects GMM,  
 17 we run a robust linear mixed-effects regressions [rlmm by Koller (2016)] independently for the 25 EAS  
 18 IMs  $f = 0.15 - 20\text{Hz}$ . Along with the fixed-effect regression coefficients and random-effect  
 19 adjustments, we produced also the fixed-effects variance-covariance matrices needed to estimate the  
 20 GMM epistemic uncertainty (Atik and Youngs 2014; Bindi et al. 2017a) and to update the GMM  
 21 coefficients in a Bayesian framework (Kowsari et al. 2019). These resources can be disseminated on  
 22 request.

## 23 5 FIXED-EFFECTS

24 The regression results comprise of fixed-effect coefficients and their covariance matrices, random-effect  
 25 values and their rlmm weights and standard errors, residuals, and variances. Similar to the GMM-SA,  
 26 outlier events, localities, regions, stations, and recordings are flagged as well. Fig.5 presents the  
 27 predicted Fourier amplitude spectra for a few scenarios of interest. In this plot, we show fixed-effects  
 28 prediction of FAS for:

- 29 i. [M4, M5.5, M7] implying events with  $M_W = 4, 5.5, 7$   
 30 ii. [Shallow, Intermediate, Deep] to illustrate the effect of  $h_D = 4, 8, 12\text{km}$  for events with depth  
 31  $D < 10\text{km}, 10\text{km} \leq D < 20\text{km}, 20\text{km} \leq D$ , respectively  
 32 iii. [Slower, Average, Faster] attenuating regions to illustrate the effect of replacing  $c_3$  in equation  
 33 (3) with  $c_{3,r} = c_3 + \delta c_{3,r}$ , with  $\delta c_{3,r} = 0, +\tau_{c3}, -\tau_{c3}$ , respectively

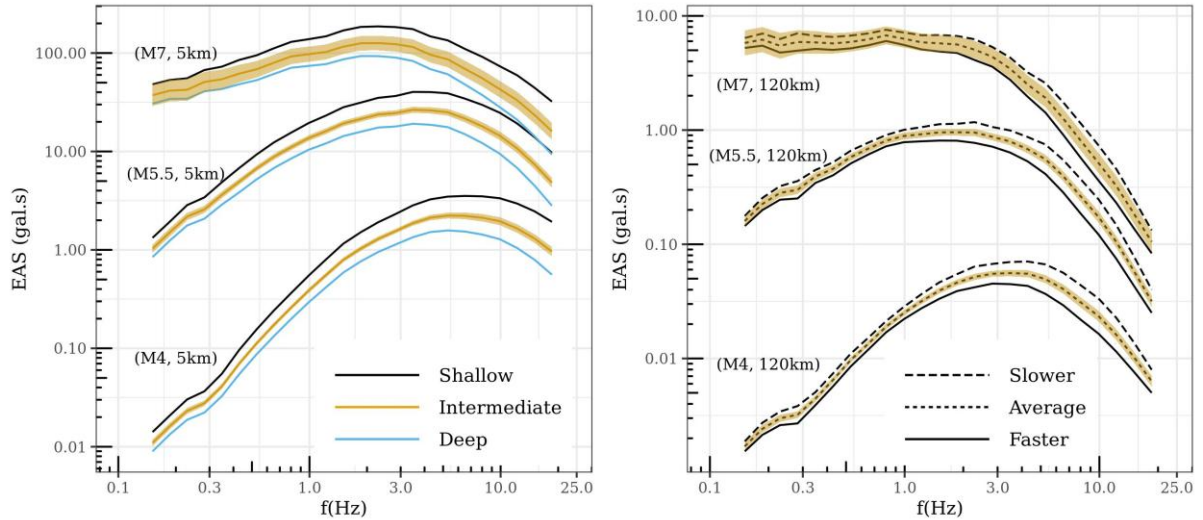


**Fig.5.** Predicted Fourier spectra of the GMM-FA for various scenarios, differentiated by color for Shallow ( $D < 10\text{km}$ ), Intermediate ( $10\text{km} \leq D < 20\text{km}$ ), and Deep ( $20\text{km} \leq D$ ) events in the left panel. In the right panel are the Fourier spectra differentiated by regional anelastic attenuation: Slower and Faster than pan-European Average

1  
2

In the left panel, showing the near-source predictions, we notice that the depth-dependence has a non-negligible effect on the amplitudes at distances  $R \leq 5\text{km}$ . For the  $(M7, 5\text{km})$  scenario, the epistemic uncertainty (orange ribbon) on the median is wide enough to cover the variation with depth. A large part of this epistemic uncertainty is from the lack of near-source data from large magnitude events, which is necessary to constrain the magnitude-scaling  $f_M(M_W)$  component of the GMM at  $M_W \geq M_h = 5.7$ .

8

In the right panel, FAS predictions at far-source distances are shown. Evidently, the  $\delta c_{3,r} = 0, +\tau_{c3}, -\tau_{c3}$  adjustments become active at  $f \geq 2\text{Hz}$  in far-source predictions. At lower frequencies, the differences are much smaller – which is to be expected since coefficient  $c_3$  is meant to capture the (apparent) anelastic attenuation of moderate-to-high frequency ground-motions.

12

Along with the depth and anelastic attenuation dependencies, we notice that with increasing magnitude the Fourier spectra become flatter in low-moderate frequency range, as the apparent corner-frequency shifts towards lower frequencies for larger magnitude events. At near-source distances (left panel), the spectra decay rapidly beyond  $f \geq 10\text{Hz}$ , while at far source distances (right panel) this behavior is observed earlier at  $f \geq 5\text{Hz}$ ; most likely from the enhanced anelastic decay of high frequency ground-motions.

18

## 6 RANDOM-EFFECTS AND RESIDUALS

19

Prior to discussing the random-effects and residuals in following sections, there are few inferences derived from the random-effect and residual variances in Fig.6. In this plot,  $\phi_{S2S}, \tau_{L2L}, \tau_0, \tau_{c3}$  are the random-effect standard deviations of between-site, between-locality (tectonic zones), between-event (after between-locality correction), and between-region (anelastic attenuation) random-variables, respectively.  $\phi$  is the residual standard deviation. The *total-sigma* of the ergodic version of GMM-FA,

23

1  $\sigma = \sqrt{\phi_{S2S}^2 + \tau_{L2L}^2 + \tau_0^2 + \phi^2}$ , does not include  $\tau_{c3}$  because it is intended for use as an epistemic  
 2 uncertainty on the anelastic attenuation term  $c_3$  of the GMM (Douglas 2018; Weatherill et al. 2020c).

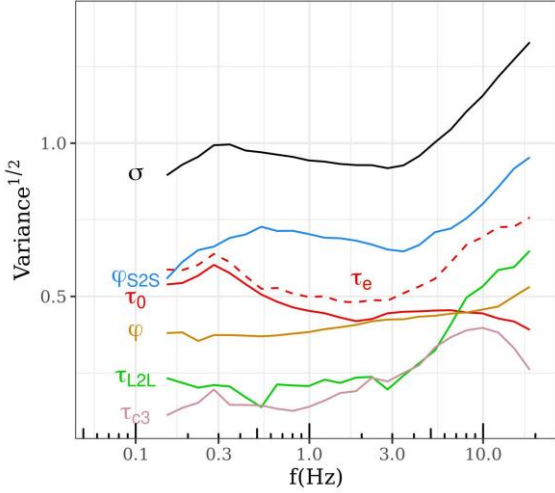


**Fig.6** Random-effect, residual, and total variance estimates of the GMM for  $f = 0.15 - 20\text{Hz}$  (solid lines), and  $\tau_e = \sqrt{\tau_0^2 + \tau_{L2L}^2}$  (dashed line)

3  
 4 All the random-variances are comparable in size, which means the random-effect groups are  
 5 meaningful for this dataset. The largest variability, however, is the site-to-site response variability -  
 6 captured by the between-site standard deviation  $\phi_{S2S}$ . Increasing monotonically at  $f \geq 3\text{Hz}$ ,  $\phi_{S2S}$   
 7 suggests that site-response (in the dataset) is highly variable at moderate-high frequencies. Such rapid  
 8 increase of  $\phi_{S2S}$  towards higher frequencies has been reported for a various datasets (Bayless and  
 9 Abrahamson 2019b; Bindi et al. 2017b; Bindi et al. 2021). For instance, ground-motion amplification  
 10 at a site with  $\delta S2S_s(f = 10\text{Hz}) = 1.5 * \phi_{S2S}(f = 10\text{Hz})$  is 20 times larger than that at a site  
 11 with  $\delta S2S_s(f = 10\text{Hz}) = -1.5 * \phi_{S2S}(f = 10\text{Hz})$ . The large variability in site-response and the  
 12 consequently large  $\phi_{S2S}$  (the largest contributor to  $\sigma$ ) suggests that partially non-ergodic site-specific  
 13 ground-motion predictions may soon become indispensable (Faccioli et al. 2015; Kotha et al. 2017;  
 14 Rodriguez - Marek et al. 2013).

15 The next largest random variance is that of between-event variability quantified into  $\tau_0$ . Note  
 16 that a part of the *overall* between-event (spatiotemporal) variability  $\tau_e$  is quantified in to the between-  
 17 locality variability  $\tau_{L2L}$ ; as in  $\tau_e = \sqrt{\tau_0^2 + \tau_{L2L}^2}$ . Apparently, variability of event-specific effects is the  
 18 highest at  $f \leq 0.5\text{Hz}$ . Seismic moment and moment-magnitude are the event-specific parameters  
 19 estimated at these frequencies. For a GMM with  $M_W$  (from EMEC catalog) as an explanatory variable,  
 20 such large between-event variability at  $f \leq 0.5\text{Hz}$  suggests large differences in observed ground-  
 21 motions between events of identical  $M_W$ . The most likely cause, to our understanding, is errors in  $M_W$   
 22 in the dataset. A few studies (Holmgren and Atkinson 2018; Kuehn and Abrahamson 2017)  
 23 demonstrated that  $M_W$  uncertainty is a contributor to the between-event variability at long period  
 24 spectral accelerations, which are analogues to low frequency Fourier amplitudes. Beyond  $f \geq 1\text{Hz}$  the  
 25  $\tau_0$  values are lower and remain almost constant.

1           The counter-part of  $\tau_0$  is the between-locality variability  $\tau_{L2L}$ , which captures the average  
 2 event-to-event variability when events are localized into seismotectonic zones ('TECTO').  $\tau_{L2L}$  values  
 3 are much smaller than  $\tau_0$  at  $f < 1\text{Hz}$ , and increase monotonically above  $\tau_0$  at  $f \geq 5\text{Hz}$ . Assuming the  
 4 errors in  $M_W$  are contained in  $\tau_0$ , we discuss the physical meaning of  $\tau_{L2L}$  in subsequent sections.

5           Region-to-region variability of anelastic attenuation is quantified into  $\tau_{c3}$ . Only the high  
 6 frequency ground-motions are attenuated exponentially with distance. Therefore,  $\tau_{c3}$  increases towards  
 7 high frequencies in Fig.6. The residual standard deviation  $\phi$ , corrected for all parametric fixed-effects,  
 8 non-parametric region, locality, and site-specific random-effects, remains almost constant across the  
 9 frequency range.

10           Fig.6 illustrates the significance of the chosen random-effect groups, and the frequency  
 11 dependence of their random-variances. It is necessary to validate the random-effects by correlating them  
 12 to a physical parameter or an index. Since the random-effects are estimated only for the regions,  
 13 localities, and sites (*levels* – as explained in Regionalisation Datasets) whose ground-motion data is used  
 14 in GMM regression, new levels with no ground-motion data cannot benefit from the non-ergodic level-  
 15 specific GMM predictions. However, correlating random-effects to a physical parameter or a geospatial  
 16 index may allow, in a limited way, predicting region, locality, and site-specific adjustments for new  
 17 levels outside the regressed dataset through the correlated parameter.

## 18   **6.1   ANELASTIC ATTENUATION VARIABILITY**

19           Anelastic attenuation of high frequency ground-motions comes into play at intermediate-far source  
 20 distances (e.g.  $R \geq 80\text{km}$ ). The coefficient  $c_3$  in GMM median captures the average rate of exponential  
 21 decay of ground-motion, while  $c_1$  captures the linear decay. Substantial correlation between  $c_3$  and  $c_1$   
 22 estimates are to be expected because they together model the decay of ground-motions with distance  
 23 (Abrahamson et al. 2014; Boore et al. 2014b; Campbell and Bozorgnia 2014). Therefore, it is more  
 24 appropriate to refer to  $c_3$  as a coefficient for *apparent* anelastic attenuation.  $\delta c_{3,r}$  is meant to capture  
 25 regional variability of this exponential decay. Fig.7 shows the frequency dependence of  $\delta c_{3,r}$  for the 45  
 26 regions identified with subscript  $r$ . The region-to-region variability is largest at  $f \geq 5\text{Hz}$ , reflecting the  
 27 large  $\tau_{c3}$  in the Fig.6.

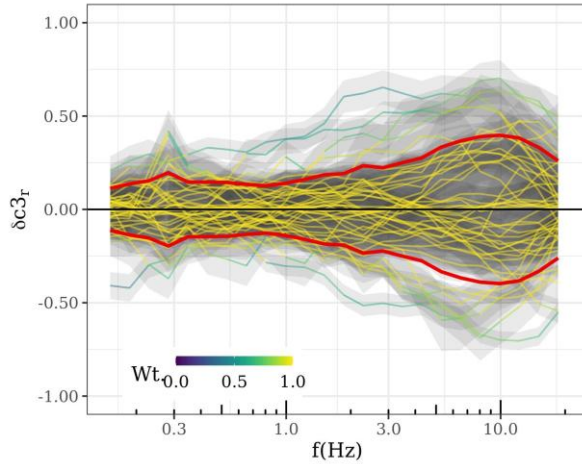


**Fig.7**  $\delta c_{3,r}$  for  $f = 0.15 - 20\text{Hz}$ . Each line corresponds to one of the 45 attenuation regions, with colors indicating their weight in robust regression. Overlain red curves mark the  $\pm\tau_{c3}$  values. Regions with  $\delta c_{3,r}(f)$  beyond  $\pm 1.345\tau_{c3}(f)$  are given a lower than a unit weight

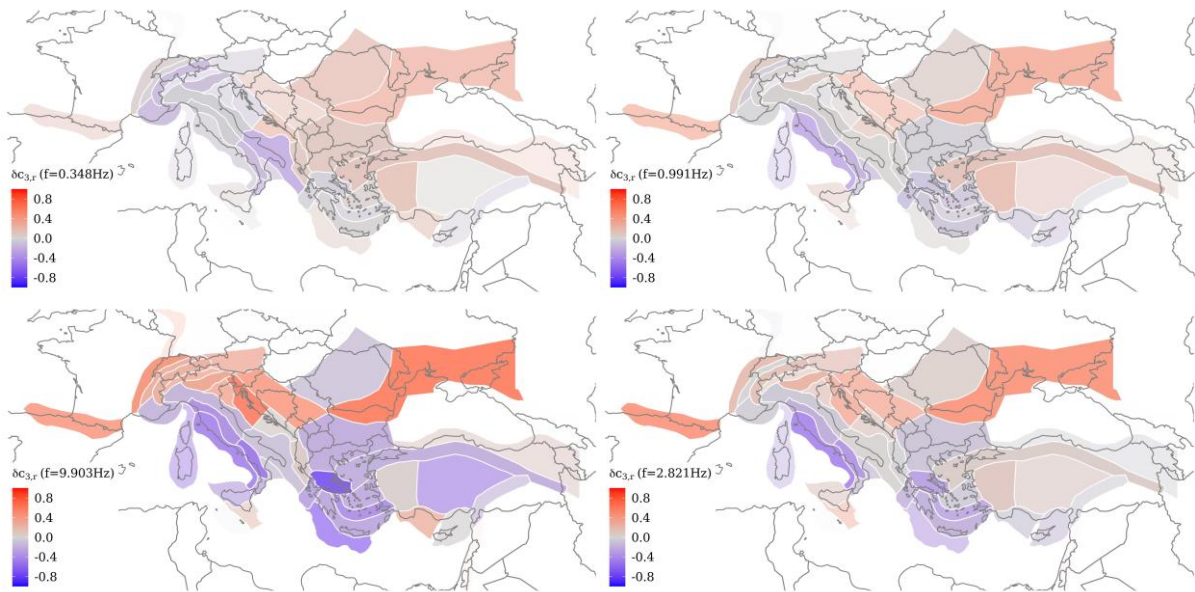
1  
2 Fig.8 maps the regional variability of  $\delta c_{3,r}$  at  $f \approx 0.3, 1, 3, 10\text{Hz}$  in the pan-European region; wherein  
3 the red colored polygons ( $\delta c_{3,r} > 0$ ) represent regions with anelastic attenuation slower/weaker than  
4 the pan-European average, and the blue colored polygons with  $\delta c_{3,r} < 0$  are those regions attenuating  
5 faster/stronger than average. Sparsely sampled regions with large epistemic uncertainty on their  $\delta c_{3,r}$   
6 are faintly colored. A few interesting remarks on these maps:

- 7 1) Weatherill et al. (2020c) showed that regions with similar attenuation characteristics, as estimated  
8 in Kotha et al. (2020), are spatially clustered. Apparently, high seismicity regions (e.g. Italy and  
9 Greece), perhaps with their highly fractured top crustal layers, attenuate the high frequency ground-  
10 motions faster/stronger than lower seismicity regions (e.g. central Europe)
- 11 2) The most well-sampled regions are located in central Italy; Northern and central Apennines W  
12 (West) with 5505 records, and Northern and central Apennines E (East) with 3199 records. While  
13 the difference is negligible at low frequencies ( $f = 0.348\text{Hz}$  top-left panel), at  $f \geq 0.991\text{Hz}$   
14 (clockwise from top-right to bottom-left panels) the difference in  $\delta c_{3,r}$  between these two regions  
15 is 0.2; which roughly translates to 10% larger ground-motion predictions at  $R = 80\text{km}$  towards  
16 east than to west. In addition to attenuating the high frequency ground-motions faster than the pan-  
17 European average, there appears to be a frequency dependent contrast between these adjacent  
18 regions.

19 Recent 3D shear wave velocity ( $V_s$ ) maps produced by Lu et al. (2018) reveal a relatively  
20 higher  $V_s$  in the Apennines (west) compared to the Adriatic basin (east) at 10km and 30km crustal  
21 depths. If we assume that a higher  $V_s$  means a higher crustal quality factor, these  $V_s$  maps would  
22 imply a more efficient propagation in the crust, which translates to slower decay towards east  
23 compared to the west. However, the spatial trends of  $\delta c_{3,r}$  indicate the contrary in this region.

24 Coincidentally, Apennines and region towards its west were reported to have shallower  
25 Moho (Grad et al. 2009) and significantly higher crustal temperatures due to submarine volcanic  
26 activity in the Tyrrhenian sea (Diaferia et al. 2019), compared to the Adriatic sea (east of  
27 Apennines); the latter phenomenon presumably better correlated to stronger attenuation of

1 mechanical waves than shear-wave velocity alone. Inopportunately, the large uncertainties in  
 2 estimates of these parameters (Moho depth and thermal gradient) at pan-European scale did not  
 3 motivate a more quantitative evaluation. Therefore, we preferred a globally available geospatial  
 4 index that is designed specifically for regionalisation of GMMs, i.e. the Activity Index in this study  
 5 3) The region in Aegean Sea attenuating fastest the high frequency ground-motions ( $f = 9.903\text{Hz}$  in  
 6 bottom-left panel) is the Gulf of Corinth, where the sites appear to have received highly attenuated  
 7 ground-motions from traversing the Aegean volcanic arc. This observation makes a strong case for  
 8 using lithosphere temperature maps to guide regionalisation of ground-motion anelastic attenuation



9 **Fig.8**  $\delta c_{3,r}$  variation across the 45 regions in ESM dataset for  $f = 0.3, 1, 3, 10\text{Hz}$  (clockwise from top-left to bottom-left panels). Blue polygons locate regions with anelastic attenuation faster than the pan-European average, red polygons locate regions with slower attenuation, and grey polygons are regions close to the average. Regions with fewer ground-motion observations, thereby larger epistemic error on  $c_{3,r}$ , are more transparent and appear fainter. Note that the color scale is the same in all the maps in order to emphasize the frequency dependence of spatial variability of anelastic attenuation

10 4) Contrast in high frequency attenuation ( $f = 9.903\text{Hz}$  in bottom-left panel) is observed around the  
 11 Alps regions, while minor differences are noticeable between west, north, and central Anatolia.  
 12 Interestingly though, the regions attenuating the slowest are the Pyrenees, the western-Balkans, and  
 13 the region north of Black sea to the east (east side of the maps here). Although not conclusive, these  
 14 regions of very slow anelastic decay coincide quite well with the regions with deepest Moho (Grad  
 15 et al. 2009); suggesting Moho depth maps could assist in regionalisation of ground-motion  
 16 attenuation (see supplement Fig.S1)

17 We note that changing the resolution or geometry of the regions may change the estimated  
 18 spatial variability and values of  $\delta c_{3,r}$  as well. However, given the current configuration, we seek  
 19 physical features that may correlate (qualitatively) with  $\delta c_{3,r}$ . A recent study by Sahakian et al. (2019)  
 20 using a large data set of small-magnitude earthquakes in Southern California suggested that crustal

1 shear-wave velocity  $V_s$  is only weakly correlated to anelastic attenuation, which also seems to be the  
 2 case here with Central Italy (observation #2 above). Regional variability of anelastic attenuation may in  
 3 fact be a combination of regional variability of crustal shear-wave velocity, crustal thermal gradient  
 4 influencing the rigidity modulus of the crust, Moho depth, and other parameters that, at the time of this  
 5 study, were not uniformly mappable across the pan-European region.

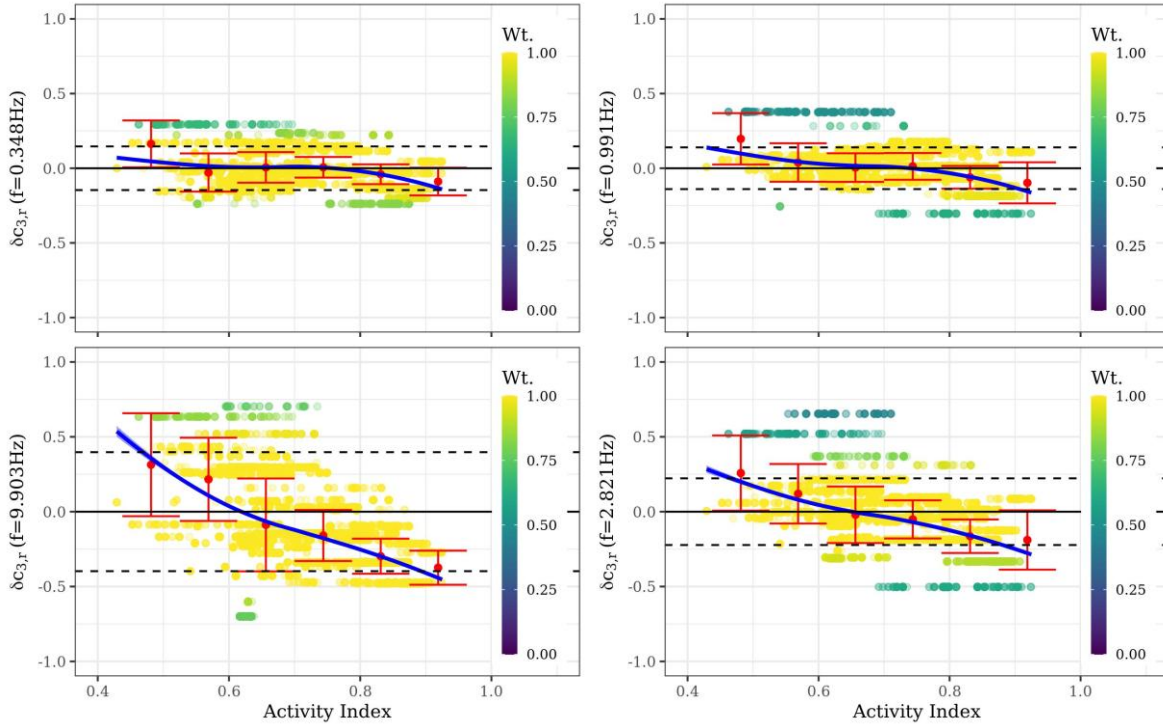


**Fig.9**  $\delta c_{3,r}$  of the 45 regions versus Activity Index at site locations within each region, for  $f \approx 0.3, 1, 3, 10\text{Hz}$  (clockwise from top-left to bottom-left). The blue lines are loess fits between the two parameters. Marker colors indicate the weight assigned to  $\delta c_{3,r}$  of each region in the rlm regression

6  
 7 Activity Index (AIx) is a unique *composite* parameter that we preferred in this study. Activity  
 8 Index is a data-driven continuous parameter inferred from a fuzzy combination of shear-wave velocity,  
 9 seismic moment rate density, and crustal quality factors across the globe. A  $0.5^\circ$  gridded map of AIx  
 10 was generated by Chen et al. (2018) for the sole purpose of regionalising GMMs or selecting suitable  
 11 GMMs for a region with no region-specific ground-motion data. In this study, we extracted the AIx for  
 12 every site location in the ESM dataset. A region with  $n$  sites will therefore have  $n$  values of AIx, which  
 13 can serve as an epistemic uncertainty on the region-specific AIx. Fig.9 shows the loess fit [non-  
 14 parametric moving average by Jacoby (2000)] between the  $\delta c_{3,r}$  of the 45 regions and the AIx of sites  
 15 located within each region. A strong negative correlation is evident at moderate-high frequencies  
 16 (bottom panels), where regional variability  $\tau_{c3}$  is the largest.

17 The negative correlation between  $\delta c_{3,r}$  and AIx in Fig.9 suggests that regions with high seismic  
 18 rate density, low shear-wave velocity, and low 1Hz coda Q (therefore, high AIx) attenuate significantly  
 19 faster than regions more likely to be cratonic (low AIx). Chen et al. (2018) indicate that the regional  
 20 variability of AIx is dominated by regional variability of seismic moment rate density in active crustal

1 regions ( $AI \geq 0.7$ ), and to that of shear-wave velocity and 1Hz code Q in relatively stable regions ( $AI <$   
 2  $0.7$ ). ESM dataset contains sites located in regions with  $0.4 \leq AI$  as seen in Fig.9. The smooth transition  
 3 of  $\delta c_{3,r}$  between stable cratonic ( $0.4 \leq AI < 0.7$ ) to the more seismically active regions ( $0.7 \leq AI \leq$   
 4  $1$ ) is an indication that it is a physically meaningful random-effect. However, these regionalisation  
 5 models are different in nature: Activity Index is fully data-driven and gridded, while the regionalisation  
 6 used in this GMM regression is based on expert elicitation and polygonised. In that sense, although there  
 7 is a decent agreement, neither of the models may sufficiently replace the other.

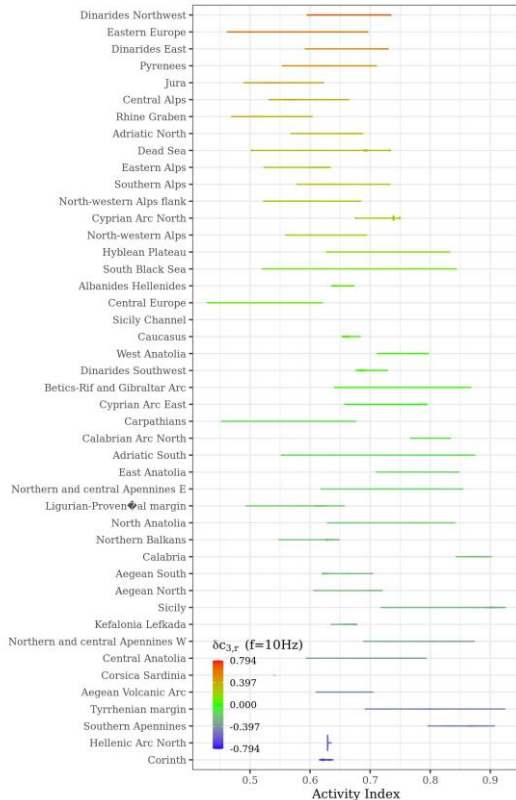


**Fig.10**  $\delta c_{3,r}$  at  $f \approx 10$ Hz of the 45 regions versus the range of Activity Index at site locations within each region

8  
 9 Fig.10 shows the ranges of AIx within each of the attenuation region. The regions are ordered  
 10 in decreasing order of  $\delta c_{3,r}(f \approx 10\text{Hz})$  from top to bottom. This figure is to illustrate the exclusivity of  
 11 the two GMM regionalisation models. For instance, the two best-sampled regions, Northern and central  
 12 Apennines W (West) and Northern and central Apennines E (East), despite their  $\delta c_{3,r}(f \approx 10\text{Hz})$   
 13 values differing by 0.2 still have significant overlap of AIx ranges i.e.  $0.68 \leq AI \leq 0.88$  and  $0.62 \leq$   
 14  $AI \leq 0.84$ , respectively. Meaning, data-driven AIx by itself may not resolve the differences between  
 15 these two adjacent regions with contrasting attenuation characteristics as efficiently as the more  
 16 subjective Basili et al. (2019) regionalisation model. In lieu of more refined and unified regionalisation  
 17 models, we foresee using both the models in correspondence to explain and predict attenuation  
 18 characteristics ( $\delta c_{3,r}$ ) for regions outside the ESM dataset. A study in this direction is anticipated with  
 19 the recently published RESIF-RAP dataset of ground-motions recorded by the French accelerometric  
 20 network (Péquegnat et al. 2008) by Traversa et al. (2020), and other low-moderate seismicity regions  
 21 whose data is not integrated into ESM.

## 1 6.2 EVENT LOCALITY VARIABILITY

2 Source variability is divided into two components in this GMM-FA: variability across tectonic localities  
 3 producing the earthquakes  $\Delta L2L \approx \mathcal{N}(0, \tau_{L2L})$ , and the locality corrected between-event  
 4 variability  $\Delta B_{e,l}^0 \approx \mathcal{N}(0, \tau_0)$ . Since events are exclusively nested in their respective tectonic localities,  
 5  $\delta L2L_l$  quantifies the *average* of the nested events' ground-motion characteristics as  $\delta B_{e,l}^0 \approx \delta B_e -$   
 6  $\delta L2L_l$ ; with notations from Al Atik et al. (2010). Fig.6 illustrates the frequency dependence of  $\tau_{L2L}$   
 7 and  $\tau_0$ . It appears that the two random-variances capture disjoint frequency dependent earthquake  
 8 characteristics; where  $\tau_0 > \tau_{L2L}$  at low-moderate frequencies, and vice versa at high frequencies.

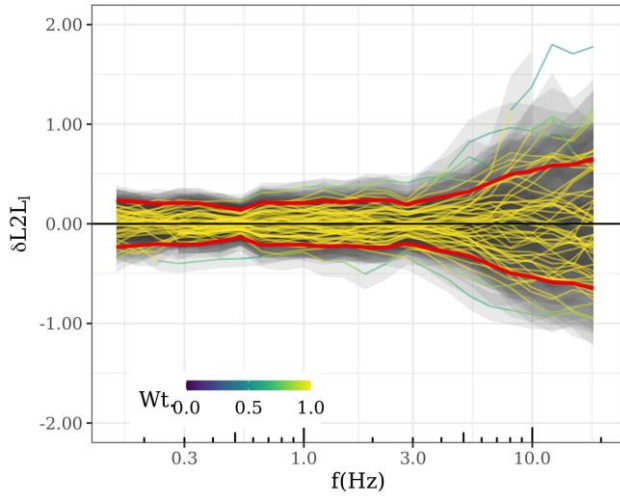


**Fig.11**  $\delta L2L_l$  for  $f = 0.15 - 20\text{Hz}$ . Each line corresponds to one of the 55 tectonic localities, with colors indicating their weight in rlm regression. Overlain red curves mark the  $\pm \tau_{L2L}$  values. Localities with  $\delta L2L_l(f)$  beyond  $\pm 1.345 \tau_{L2L}(f)$  are given a weight lower than one

9

10 Fig.11 shows the  $\delta L2L_l(f = 0.15 - 20\text{Hz})$  of the 55 tectonic localities in ESM dataset.  
 11 Resembling Fig.6, the scatter of  $\delta L2L_l$  significantly increases at  $f \geq 5\text{Hz}$  in Fig.11. The epistemic  
 12 uncertainty of  $\delta L2L_l$ , i.e. the standard-error  $SE(\delta L2L_l)$ , are generally smaller than  $\tau_{L2L}$ . In this regard,  
 13 dropping  $\tau_{L2L}$  from the aleatoric variability ( $\sigma$ ) and using instead the  $\delta L2L_l \pm SE(\delta L2L_l)$  adjustments  
 14 to regionalise the GMM predictions is recommended. A database of  $\delta L2L_l$ ,  $SE(\delta L2L_l)$ , and their rlm  
 15 weights indicating outliers can be provided on request for analyses and applications. For instance, Fig.11  
 16 suggests that the number of detected outliers increases towards higher frequencies, along with  $\tau_{L2L}$ . A  
 17 few of these outliers are also well-sampled localities with a low  $SE(\delta L2L_l)$ ; implying a more source  
 18 specific study could be worthwhile.

19 Fig.12 maps the various tectonic localities (indexed  $l$ ) color coded to their  $\delta L2L_l(f \approx$   
 20  $0.3, 1, 3, 10\text{Hz})$  values. The colors in panel corresponding to  $f \approx 0.3, 1\text{Hz}$  (in the top row) are fainter  
 21 compared to those of  $f \approx 3, 10\text{Hz}$  (bottom right and left, respectively); indicating the greater diversity  
 22 in source characteristics and the larger  $\tau_{L2L}$  in Fig.6. In the bottom-left panel showing spatial variability  
 23 of  $\delta L2L_l(f \approx 10\text{Hz})$ , a strong contrast in source characteristics between central Italy and western  
 24 Anatolia is apparent. This means that, despite being of similar magnitude, earthquakes originating in  
 25 central Apennine fault systems generated substantially lower high frequency ground-motions than those  
 26 originating in north-western segment of Anatolian fault (near Istanbul, Turkey).

1

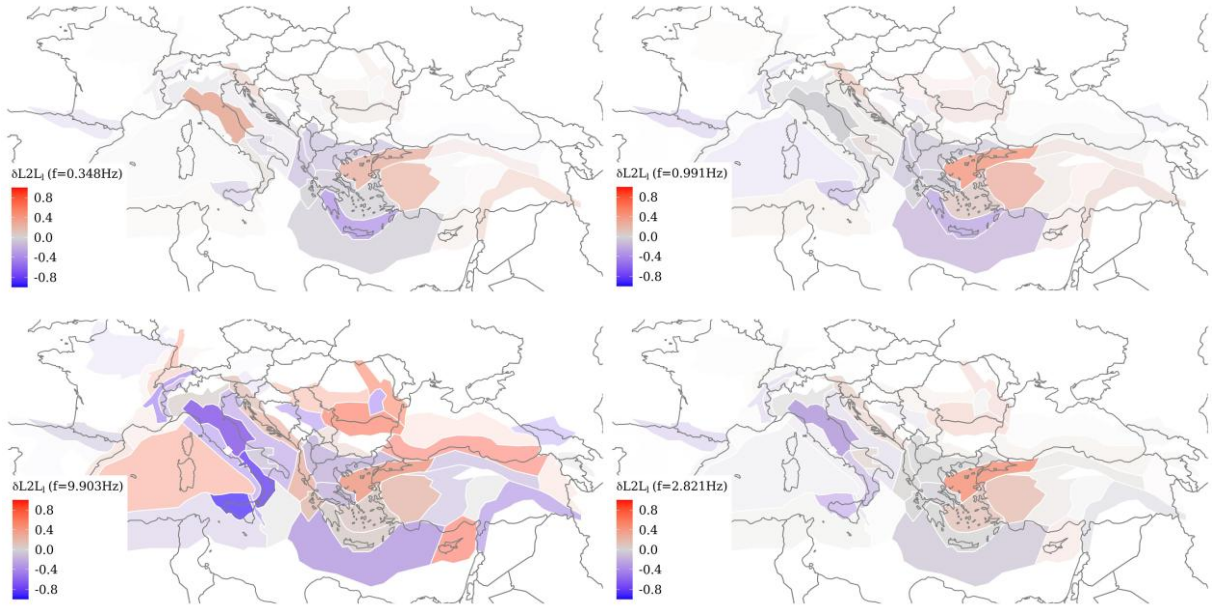


**Fig.12** Tectonic localities and the  $\delta L2L_l$  for these locality polygons. Red colored localities produced events capable of higher  $GM(f = 0.3, 1, 3, 10\text{Hz})$  than the GMM median predictions, blue colored localities produced earthquakes weaker than dataset average, and grey colored localities are close to the dataset average. Localities with fewer ground-motion observations, thereby larger epistemic error on  $\delta L2L_l$ , are more transparent and appear fainter. Note that the color scale is the same in all the maps in order to emphasize the frequency dependence of spatial variability of event characteristics

2

3

4

5

6

7

8

9

10

11

12

13

14

15

16

17

18

19

20

21

Similar but lower contrast is apparent when comparing the  $\delta L2L_l(f \approx 10\text{Hz})$  of central Apennines and Po-plain tectonic localities. The M6.5 Norcia earthquake and associated shocks (in 2016), and several well studied past earthquake sequences (e.g. L'Aquila sequence of 2009) originated in this central Apennines tectonic locality. On the other hand, the substantially stronger (with higher stress-drop) M6.45 Friuli earthquake (in 1976) and a few recent earthquakes are allotted to the Po-plain tectonic locality. Initially, we have considered that the spatial trends (of  $\delta L2L_l$ ) in Fig.12 reflect the differences in observed ground-motions as governed by the predominant focal mechanisms in these localities. However, the within-locality diversity of focal mechanisms dissuaded us from this hypothesis.

It is important to note that the color scale ranges in Fig.12 are not frequency dependent. Despite, an interesting feature in Fig.12 is the inversion of  $\delta L2L_l$  in the central Apennines from positive values at  $f \approx 0.3\text{Hz}$  to negative values at  $f \approx 10\text{Hz}$  (red to blue color). It is however inconclusive if the events in this region produced low frequency ground-motions stronger than pan-European average or if it is the inhomogeneity of  $M_W$  estimates across the pan-European region that is being captured by the  $\delta L2L_l$  at  $f \leq 0.3\text{Hz}$ .

We have already seen in Fig.9 the clear correlation between  $\delta c_{3,r}$  and the  $A_{ix}$  values at station locations. Fig.13 is similar in description to Fig.9, but instead of  $A_{ix}$  at each station location within an attenuating region, we use the  $A_{ix}$  at event locations within a tectonic locality. Although not presented here, we found no correlation between  $\delta B_{e,l}^0$  vs  $A_{ix}$  at any frequency (see supplement Fig.S6). It means to say that when  $\delta B_{e,l}^0$  variability is large within a tectonic locality, the much larger localities composed

1 of several  $0.5^\circ$  grid cells with similar  $AIx$  values are unlikely to resolve event-specific differences. On  
 2 the other hand, the size of tectonic localities is comparable to the size of regions with distinguishable  
 3  $AIx$  values (Fig.4). As a result, Fig.13 shows an interestingly strong relationship between  $\delta L2L_l$  and  
 4  $AIx$  (at event locations).

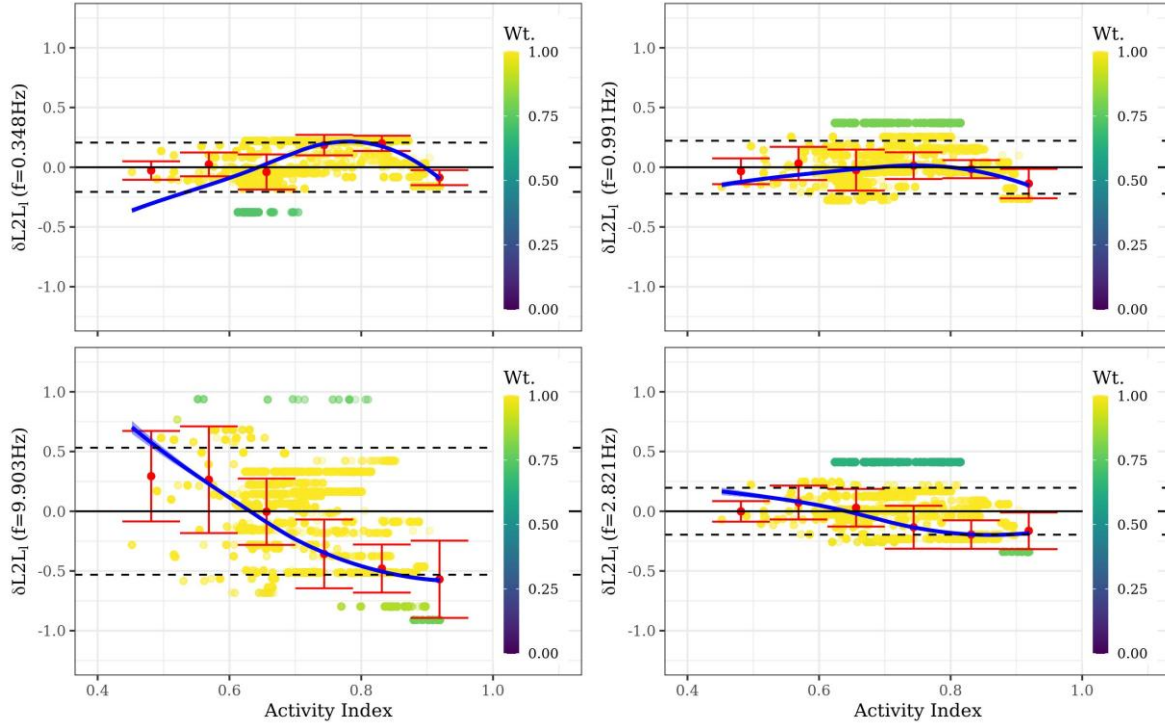


**Fig.13**  $\delta L2L_l$  of the 55 tectonic localities versus  $AIx$  at event locations within each locality, for  $f = 0.3, 1, 3, 10\text{Hz}$  (clockwise from top-left to bottom-left). The blue lines are loess fits between the two parameters. Marker colors indicate the weight assigned to  $\delta L2L_l$  of each locality in the rlm regression

5  
 6 Up to  $f \approx 1\text{Hz}$ , we observed no resolvable trends between  $\delta L2L_l$  and  $AIx$ . Moving towards  
 7 higher frequencies, as  $\tau_{L2L}$  gains relevance, a significant negative correlation is observed. Essentially,  
 8 the loess fits for  $f \geq 2\text{Hz}$  suggest that the tectonic localities coinciding with regions with  $AI \geq 0.7$  are  
 9 more likely to produce, on average, weaker high frequency ground-motions than those with  $AI < 0.7$ .  
 10 However, since  $AIx$  is a fuzzy combination of three physical parameters, it is not obvious which one is  
 11 responsible for the negative correlation with  $\delta L2L_l$  (see supplement Fig.S2 for correlation with seismic  
 12 moment rate density).

13 A classical hypothesis has been that events in stable continental regions produce stronger high  
 14 frequency ground-motions than those in active crustal regions by virtue of their larger stress-drops, e.g.  
 15 Bommer et al. (2015). In this case, stable continental regions are those with lower  $AIx$  and appear to  
 16 coincide with tectonic localities with higher  $\delta L2L_l$  values in Fig.13. Alternatively, the large  $\tau_{L2L}$  value  
 17 at high frequencies could be from regional variability of a high frequency source parameter, e.g. the  
 18  $\kappa^{source}$ ; which is the high frequency decay parameter of Brune's  $\omega^2$  source model (Bindi et al. 2019b).  
 19 Bindi and Kotha (2020) estimated the  $\kappa^{source}$  of several events in the ESM dataset, but the large  
 20 variability of, and uncertainty in, deter us from associating these estimates with the already uncertain

1  $\delta L2L_l$ . Although not reported here, we do observe a reasonable positive correlation between  $\kappa^{source}$   
 2 and Aix (see supplementary figure).

3 Through an exploratory analysis, we deduced a third hypothesis by comparing the three best-  
 4 sampled localities in: central Appenines of Italy (“PTTC007” -  $\delta L2L_l(f = 10\text{hz}) = -0.6$ ), north-west  
 5 segment (“SETC003” -  $\delta L2L_l(f = 10\text{hz}) = 0.3$ ), and the north-east segment of Anatolian fault system  
 6 (“AMTC001” -  $\delta L2L_l(f = 10\text{hz}) = -0.3$ ). These three regions have similar seismic moment rate  
 7 density, 1 Hz coda  $Q_0$ , and shear wave velocity variation at 175km depth, and therefore, similar Aix  
 8 values (see Fig.4). These tectonic localities produced several  $M_W \geq 6$  earthquakes as well. Bindi and  
 9 Kotha (2020) showed that the stress-drop estimates for the large events in north-west Anatolia are a  
 10 magnitude higher than those of the central Appenines; while those of north-east Anatolia were  
 11 unconstrained due to lack of sufficient station coverage. Perrin et al. (2016) showed that the structurally  
 12 immature north-west Anatolia produced large earthquakes with systematically lower rupture speed than  
 13 those originating in the structurally mature north-east Anatolian segment. Chounet et al. (2018) followed  
 14 up with a global database showing an anticorrelation between stress-drop and rupture speed. An earlier  
 15 study by Radiguet et al. (2009) connected the lower near-field ground-motions (e.g. peak ground  
 16 acceleration) to structural maturity of fault systems. Based on these studies, we infer that the  
 17 structurally immature fault segments produced earthquakes capable of stronger high frequency ground-  
 18 motions. In this study, we concur with the hypothesis that the younger, westward growing north-west  
 19 Anatolian fault system produced stronger earthquakes than the older, north-east Anatolian and central  
 20 Appenine fault systems.

21 In summary,  $\delta L2L_l$  is introduced to capture partially, in a predictable way, the spatial variability  
 22 of event dependent ground-motion variability. While the location corrected event-specific  $\delta B_{e,l}^0$  retains  
 23 a large party of event-to-event stress-drop variability as shown in Bindi et al. (2019b);  $\delta L2L_l$  captures  
 24 the average regional trends, which in-turn appear to be controlled by macroscopic fault system  
 25 characteristics – and not necessarily by the stress-drop (see supplementary Fig.S4). Given its strong  
 26 correlation with Activity Index, we hypothesize that the trends shown in Fig.13 may assist in *guessing*  
 27 an appropriate  $\delta L2L_l$  for low-moderate seismicity regions (e.g. France and Germany) whose ground-  
 28 motion data is absent in ESM i.e., more positive  $\delta L2L_l$  in regions with lower Aix values (in Fig.4)

### 29 **6.3 EVENT VARIABILITY**

30 Bindi and Kotha (2020) and a few earlier studies demonstrated a strong correlation between the  
 31 traditional between-event random-effect  $\delta B_e$  and stress-drop. We found a similarly strong correlation  
 32 between the  $\delta L2L_l$  corrected between-event random-effect  $\delta B_{e,l}^0$  and stress-drop here as well  
 33 (supplement Fig.S5) – but no correlation with *AI* (supplement Fig.S6). Stress-drop is not quite the  
 34 spatiotemporally predictable parameter, and can be quite variable within any tectonic locality. However,  
 35 it is commonly acknowledged that ground-motion variability among large magnitude events is smaller

1 than small events. This has been verified by Youngs et al. (1995) as a magnitude dependence of ground-  
 2 motion variability – irrespective of sample size. Several subsequent GMM-SAs have since featured the  
 3 so-called heteroskedastic between-event variance ( $\tau_e$ ) models.

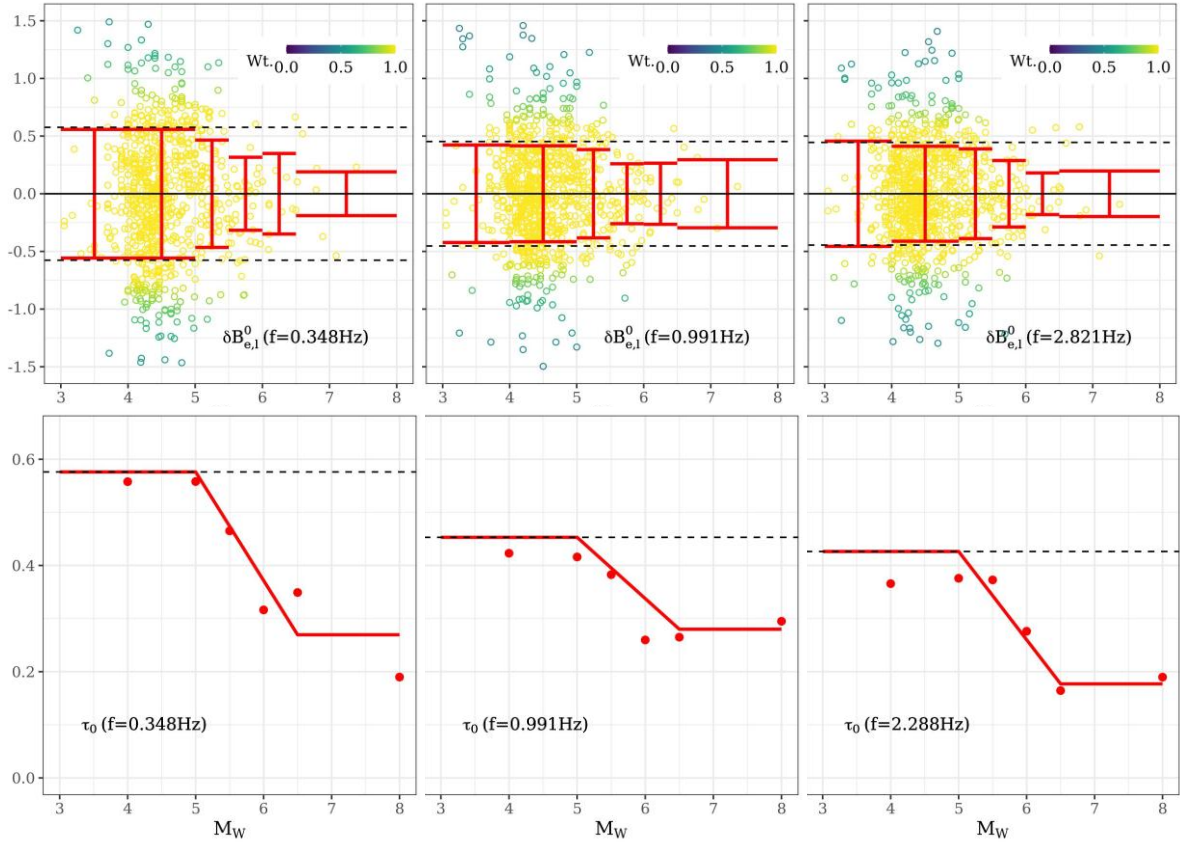


**Fig.14** Magnitude and frequency dependent heteroskedasticity of between-event variability  $\tau_0$ . Top row panels show  $\delta B_{e,l}^0 \sim M_W$  at  $f \approx 0.3, 1, 3\text{Hz}$ , wherein the marker colors are rlm weights, black dotted lines delimit  $\pm \tau_0$ , and red error bars indicate the Median Absolute Deviation (MAD) in  $M_W$  bins (details in main text). Bottom row panels show the fitted magnitude dependent  $\tau_0$  in red against the black dashed line of homoskedastic  $\tau_0$

4

5 Magnitude-dependent heteroskedasticity of  $\tau_e$  makes physical sense because larger ruptures  
 6 tend to occur more-or-less on the same area of the fault plane, and periodically release a similar amount  
 7 of accumulated elastic energy or stress. However, if the large events of similar magnitude originate in  
 8 fault systems (or tectonic localities) with very different stress accumulation and release rates, the  
 9 variability of stress-drop (and the  $\delta B_e$ ) could be as large as that of smaller events. This means that,  
 10 heteroskedasticity of  $\tau_e$  in a global dataset consisting of events from Italy, Turkey, Japan, China, etc.,  
 11 (e.g. NGA-West2) may not be as significant as that of events within a tectonic locality within any of  
 12 these geopolitical boundaries. In our case, we remove the locality-to-locality variability of event  
 13 characteristics through the random-effect  $\Delta L2L_l = \mathcal{N}(0, \tau_{L2L})$ , leaving us a large sample of  $\Delta B_{e,l}^0 =$   
 14  $\mathcal{N}(0, \tau_0)$  that can be examined for a generic heteroskedasticity with  $M_W$ , independent of events'  
 15 localities. Based on this understanding, we have modeled a frequency and  $M_W$  dependent  
 16 heteroskedastic  $\tau_0$ , as illustrated in Fig.14

1 In the top panel of Fig.14, we show the  $\delta B_{e,l}^0 \sim M_W$  color coded by their rlmm weights. Overlain  
 2 on the scatter plot are error-bars (in red), which bound  $\pm MAD$  (median absolute deviation) of  $\delta B_{e,l}^0$   
 3 binned according to  $M_W \in [3.4, 4), [4,5), [5,5.5), [5.5,6), [6,6.5), [6.5,7.4]$ . As in most GMM-SAs, our  
 4 GMM-FA between-event variability decreases with increasing  $M_W$ . At  $M_W < 5$ , the  $MAD$  is  
 5 comparable to the  $\tau_0$ , while at  $M_W \geq 6.5$  the  $MAD$  is on average 50% smaller than  $\tau_0$  – depending on  
 6 the frequency. In the lower panels of Fig.14, we show the estimated  $M_W$  binwise  $MAD$  (red markers),  
 7 and the piece-wise linear model of heteroskedastic between-event variability, shown in equation (5).

$$\tau_0(M_W) = \begin{cases} \tau_{0,M_1} = \tau_0 & M_W < M_1 = 5 \\ \tau_{0,M_1} + (M_W - M_1) \left( \frac{\tau_{0,M_2} - \tau_{0,M_1}}{M_2 - M_1} \right) & M_1 \leq M_W < M_2 = 6.5 \\ \tau_{0,M_2} & M_W \geq M_2 \end{cases} \quad (5)$$

8 In equation (5), for each frequency ( $f$ , not shown in equation),  $\tau_{0,M_1}$  is the between-event  
 9 variability for events with  $M_W < M_1 = 5$ , which is set equal to  $\tau_0$ . For large events with  $M_W \geq M_2 =$   
 10 6.5, the between-event variability is a smaller  $\tau_{0,M_2}$ . For  $M_1 \leq M_W < M_2$ , the between-event variability  
 11 decreases linearly from  $\tau_{0,M_1}$  to  $\tau_{0,M_2}$ . Values of these parameters are provided in the supplementary  
 12 coefficient table.

#### 13 6.4 SITE-RESPONSE VARIABILITY

14 The next, and by far the largest, random variability is the site-response component  $\delta S2S_s = \mathcal{N}(0, \phi_{S2S_s})$ .  
 15 Fig.6 shows that  $\phi_{S2S_s}$  is consistently the largest random-variance at all frequencies, when measured as  
 16 site-to-site ground-motion variability across the 1622 sites in ESM dataset. Site-specific ground-motion  
 17 predictions are more accurate and precise (smaller aleatory variability) than ergodic or region-specific  
 18 predictions, but are only possible when site-specific ground-motion data are available. In absence of  
 19 site-specific observations, site-response proxies are necessary to extrapolate spatially the site-specific  
 20 terms  $\delta S2S_s$  (Kotha et al. 2018; Weatherill et al. 2020b). For such studies, we disseminate a database of  
 21  $\delta S2S_s(f = 0.15 - 20Hz)$  derived from the ESM dataset.

22 Fig.15 shows the relation of  $\delta S2S_s(f \approx 0.3, 1, 3, 10Hz)$  with measured  $V_{s30}$  (left column), and  
 23 topographic slope (right column). While only 400 sites are provided with measured  $V_{s30}$  in the ESM  
 24 dataset, topographic slope is available at all site locations. In Fig.15, each marker corresponds to a site  
 25 with an estimated  $\delta S2S_s$  (irrespective of number of records), color coded to their rlmm weight. The  
 26 error-bars (red) illustrate the mean and  $MAD$  within each Eurocode 8 site-class. The blue curve  
 27 represents the proposed linear soil-response model, derived as a quadratic function of  $V_{s30}$  or slope.  
 28

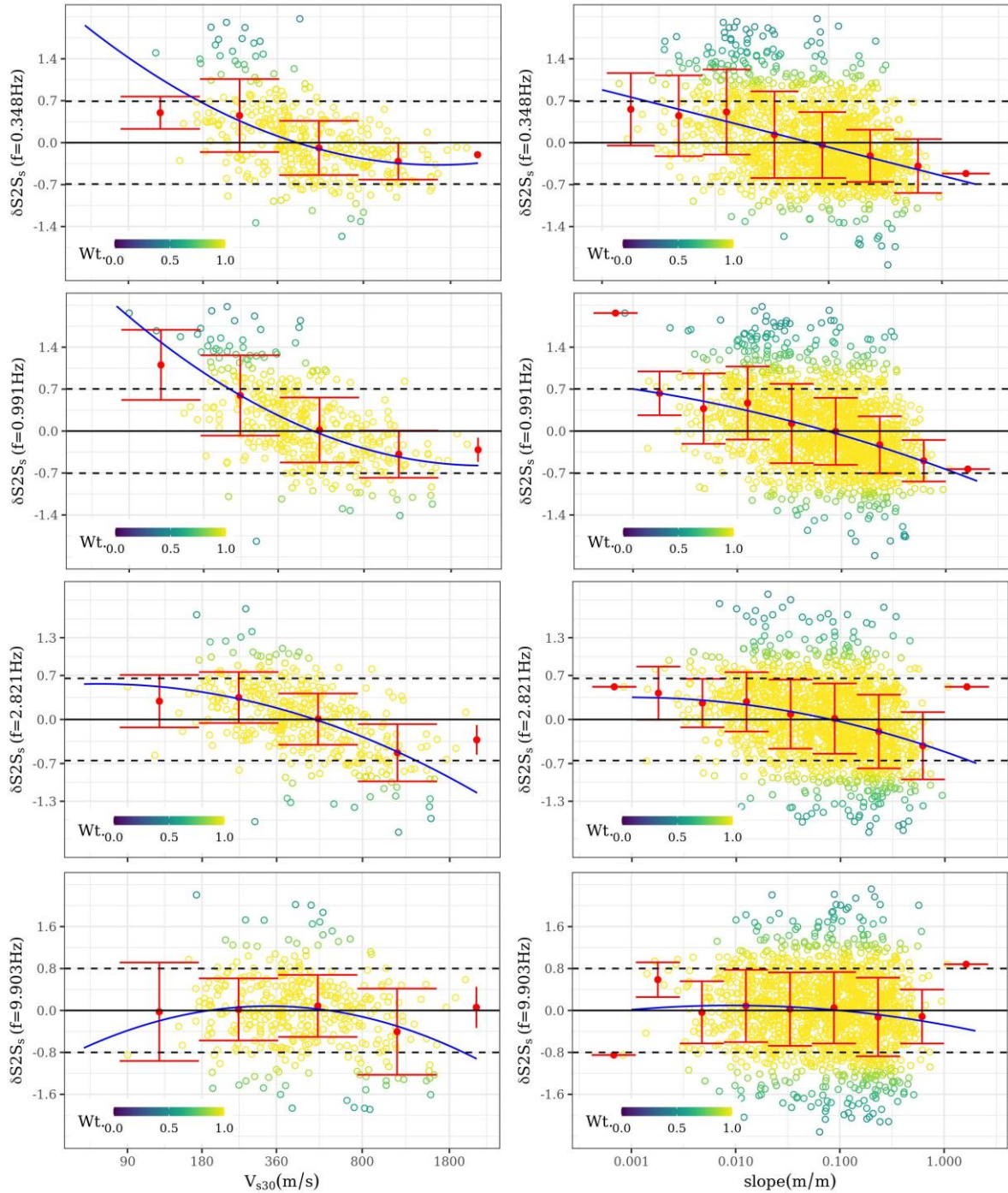


**Fig.15** Plot showing the trend of  $\delta S2S_s(f \approx 0.3, 1.3, 10\text{Hz})$  (from top to bottom rows) with  $V_{s30}$  (left column) and topographic slope at site location (right column). Note that only 400 sites have measured  $V_{s30}$  in the ESM dataset, while all 1622 sites have topographic slope values.

1

2

3

4

5

6

7

Looking at the  $\delta S2S_s$  trends with  $V_{s30}$ , it is evident that sites in EC8 class D ( $V_{s30} \leq 180\text{m/s}$ ) and class C ( $180 < V_{s30} \leq 360\text{m/s}$ ) significantly amplify low frequency ground-motions compared to the average of the dataset. In addition, the within class site-to-site variability (error-bar) is apparently larger than that of EC8 class B ( $360 < V_{s30} < 800\text{m/s}$ ) and A ( $800\text{m/s} < V_{s30}$ ). The site-response of class A sites does not appear to scale with  $V_{s30}$  at low frequencies. The converse is observed at high frequencies, wherein, class A and B sites exhibit higher site-to-site variability, and scale steeply with

1  $V_{S30}$ . Interestingly, the flattening of  $f \approx 3, 10\text{Hz}$  site-response function (blue curve) towards lower  $V_{S30}$   
 2 suggests that class C and D sites exhibit high frequency amplifications lower than that a linear  $V_{S30}$   
 3 scaling function would predict. Although this is likely from nonlinear behavior of soft soils when  
 4 subjected to strong input ground-motion, a further record-to-record investigation is necessary.  
 5 Alternatively the left-over residuals at these sites can be examined for nonlinear soil response, as in  
 6 Loviknes et al. (2021).

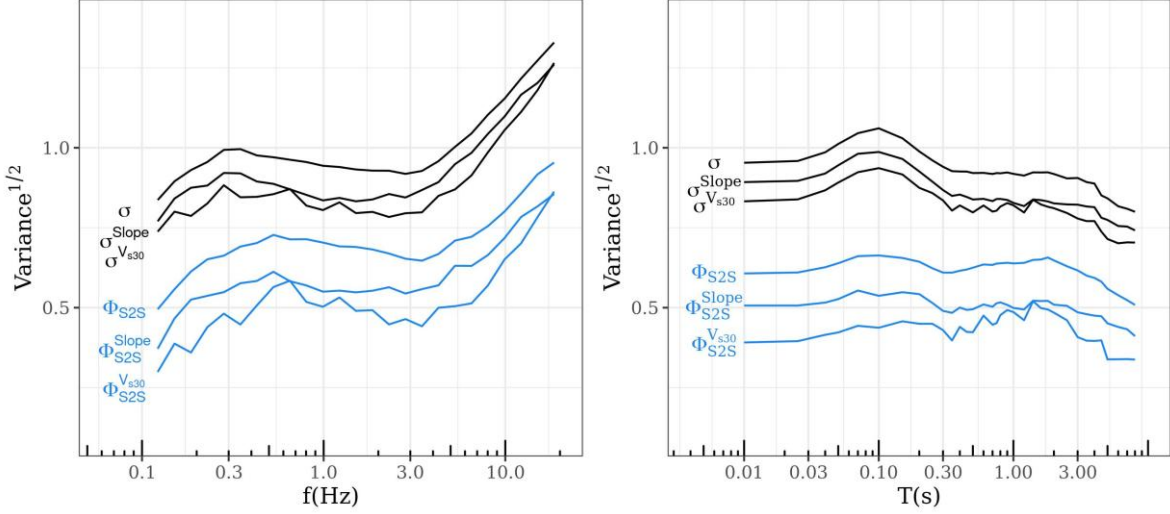


**Fig.16** Between-site and total variance estimates ( $\phi_{S2S}, \sigma$ ) of the GMM-FA for  $f = 0.15 - 20\text{Hz}$  (in left-panel) and of the Kotha et al.(2020) GMM-SA for  $T = 0.01 - 8\text{s}$  (in right-panel), along with the reduction in ( $\phi_{S2S}, \sigma$ ) to ( $\phi_{S2S}^{V_{S30}}, \sigma^{V_{S30}}$ ) when using  $V_{S30}$ , and to ( $\phi_{S2S}^{slope}, \sigma^{slope}$ ) when using  $Slope$  as site-response proxies

7  
8  
9  
10  
11  
12  
13  
14  
15  
16  
17

For now, we only provide the site-response ( $SR^{V_{S30}}, SR^{slope}$ ) as quadratic functions of  $V_{S30}$  and slope, along with a database of site-response terms, as in equations (6) and (7). Here, the measured  $V_{S30}$  is in  $m/s$  and  $slope$  in  $m/m$ , the regression coefficients  $g_0, g_1, g_2$  are different for  $SR^{V_{S30}}$  and  $SR^{slope}$ , and change with frequency. Robust linear fits using an M estimator (Venables and Ripley 2002), at each of 25 frequencies between  $f = 0.15\text{Hz} - 20\text{Hz}$ ,  $PGA$  ( $T = 0\text{s}$ ) and  $PGV$ , are derived for  $\delta S2S_s \sim V_{S30}$  correlation of 400 sites with measured  $V_{S30}$  available, and  $\delta S2S_s \sim slope$  of the 1622 sites with  $slope$  derived from digital elevation models provided by Shuttle Radar Topography Mission (Jarvis et al. 2008). The residuals from  $\delta S2S_s \sim V_{S30}$ (measured) and  $\delta S2S_s \sim slope$  regressions are  $\delta S2S_s^{V_{S30}}$  and  $\delta S2S_s^{slope}$ , with robust standard-deviations  $\phi_{S2S}^{V_{S30}}$  and  $\phi_{S2S}^{slope}$ , respectively. All the coefficients and standard-deviations are provided in the supplementary coefficient table.

$$SR^{V_{S30}} = g_0 + g_1 \cdot \ln\left(\frac{V_{S30}}{800}\right) + g_2 \cdot \left(\ln\left(\frac{V_{S30}}{800}\right)\right)^2 \quad (6)$$

$$SR^{slope} = g_0 + g_1 \cdot \ln\left(\frac{slope}{0.1}\right) + g_2 \cdot \left(\ln\left(\frac{slope}{0.1}\right)\right)^2 \quad (7)$$

18 Slope is a poorer explanatory parameter of site-response than measured  $V_{S30}$ , but is relatively  
 19 easier to obtain at any site location. The left panel of Fig.16 shows the reduction in  $\phi_{S2S}$  from using

1  $V_{s30}$  and slope as site-response proxies in the GMM-FA. Although the reduction at lower frequencies is  
 2 substantial, an explanation for the large variability of high frequency site-response is still evasive. A  
 3 few studies, e.g. Hollender et al. (2020), Mucciarelli et al. (2017), and Stewart (2000), discussed the  
 4 impact of instrument housing and soil-structure interaction on ground-motion recordings; which might  
 5 explain the relatively large site-to-site response variability at high frequencies, even among sites with  
 6 similar  $V_{s30}$ , compared to that at lower frequencies.

7 Also shown in this figure, in the right panel, is the reduction in  $\phi_{s2s}$  from using  $V_{s30}$  and slope  
 8 as site-response proxies in the GMM-SA of Kotha et al. (2020). While the variances at  $f \leq 3\text{Hz}$  and  
 9  $T \geq 0.3\text{s}$  are comparable, the ground-motion variability at short periods (e.g.  $T < 0.3\text{s}$ ) captured by  
 10 GMM-SA is a severe underestimate of the actual variability of high frequency ground-motions (e.g.  $f >$   
 11  $3\text{Hz}$ ). Differences as such were also observed while comparing the between-locality and between-region  
 12 random-variances  $\tau_{L2L}$  and  $\tau_{c3}$ , respectively. This observation reinforces the importance of GMM-FAs  
 13 over GMM-SAs in the various practical applications we highlighted in the Introduction section, and also  
 14 our motivation to evaluate the physical meaning of between-region  $\Delta c_{3,r}(f)$  and between-locality  
 15  $\Delta L2L_l(f)$  random-effects in Fourier domain instead of in response spectral domains – especially at high  
 16 frequencies, where their variances are largest (see Fig.6). In case of the between-locality and between-  
 17 region random-effect groups, the correlations  $\delta L2L_l \sim AI$  in Fig.13 and  $\delta c_{3,r} \sim AI$  in Fig.9 explain to a  
 18 good extent the large  $\tau_{L2L}$  and  $\tau_{c3}$  values at high frequencies. But the large  $\phi_{s2s}$  at high frequencies  
 19 could not be resolved using Activity Index. As stated above, the variability of site-response at high  
 20 frequencies could be from instrument housing type or more physical; such as the influence of deeper  
 21 soil layers, plasticity of soil column, weathering of bedrock, seasonal changes in shear-wave velocity in  
 22 shallow layers (Alexis et al. 2021; Roumelioti et al. 2020), etc. However, in-lieu of resolving such issues,  
 23 and given the practical importance of high frequency site-response, the most efficient solution yet is to  
 24 collect more site-specific data (Bard et al. 2019).

25 Apart from the random-effects analyses presented in the previous section, customary checks for  
 26 magnitude and distance dependencies showed no peculiarities – therefore, we skip presenting them here.  
 27 Finally, the aleatoric ‘left-over’ residuals can be examined for evidences of some secondary  
 28 phenomenon which are record-specific and are not captured by the mixed-effects such as: shear-wave  
 29 radiation pattern in near-source distances (Kotha et al. 2019), SmS reflections at intermediate- and far-  
 30 source distances (Bindi and Kotha 2020; Bindi et al. 2006), nonlinear soil response (Loviknes et al.  
 31 2021), etc. However, each of these phenomena require information that are not currently available in  
 32 the ESM dataset (e.g. centroid-moment-tensor solutions and crustal shear-wave velocity profiles). For  
 33 sake of brevity of the manuscript, we anticipate in-depth residual analyses to follow-up studies.

## 7 DISCUSSION

1  
2 We presented in this study a ground-motion model capable of predicting Fourier amplitudes in the  
3 frequency range  $f = 0.15 - 20\text{Hz}$ . This model is developed as complementary to the regionally  
4 adaptable ground-motion model for response spectra predictions by Kotha et al. (2020). Hence it's  
5 applicability range and application strategy are the same as those described in Kotha et al. (2020) and  
6 Weatherill et al. (2020c). However, unlike Bayless and Abrahamson (2019b), we have not smoothed the  
7 fixed-effects coefficients to extend the applicability range of our model. Therefore, we advice against  
8 extrapolating the model to higher or lower frequencies. The random-effect and residual variances of our  
9 model are large, but are still comparable to the recent models by Stafford (2017) and Bora et al. (2019).  
10 Interestingly, all these models' variances show striking similarity in the rapid increase of estimated  
11 ground-motion variability at the high frequencies – a feature that is completely masked in the variance  
12 estimates of response spectra ground-motion model.

13         The three types of partial non-ergodicity are captured by three random-effect groups: between-  
14 locality, between-region, and between-site. Random-variances of all three groups increase rapidly at  
15  $f > 3\text{Hz}$ . This intriguing feature was not apparent in the random-variances of Kotha et al. (2020) at  
16 periods  $T < 0.3\text{s}$ . Therefore, we found it more appropriate to evaluate the physical meaning of between-  
17 locality and between-region random-effects in Fourier domain, which is more closely related to actual  
18 physics of seismic ground-motion than the response spectral domain. We have attempted correlating  
19 these random-effects to a suite geological and geophysical parameters, but have not reported them here  
20 for various reasons – and of course for the sake of brevity. The most convincing correlation, however,  
21 was with Activity Index of Chen et al. (2018). This fuzzy logic based transparent and data-driven  
22 geospatial index is able to resolve the high between-locality and between-region random-variances at  
23 high frequencies. Our interpretation is that regions with high Activity Index (high seismic moment rate  
24 density, low 1HZ coda Q, low crustal shear-wave velocity at 175km) attenuate the high frequencies  
25 much faster/stronger than regions with low Activity Index (low seismic moment rate density, high 1HZ  
26 coda Q, high crustal shear-wave velocity at 175km). Similarly, tectonic localities characterised by low  
27 Activity Index (e.g. moderate seismicity regions like France) produced more energetic earthquakes, on  
28 average, compared to localities with high Activity Index (e.g. high seismicity regions like central Italy).  
29 Activity Index as a composite parameter correlates better to the spatial variability of between-locality  
30 and between-region random-effects, than its componentes individually.

31         Nevertheless, we find a strong potential in Activity Index as regionalisation parameter in our  
32 future ground-motion models. There are several directions we foresee: (1) using Activity Index as  
33 *regionalizing* fixed-effect in ground-motion models, (2) using Activity Index to adapt the between-  
34 locality and between-region random-effects to sparsely sampled low seismicity areas, and (3) upgrading  
35 the Activity Index with newer/updated maps of Moho depth, lithospheric temperature, crustal shear-

1 wave velocity maps, etc. The direction (2) is already on course using the recently published ground-  
2 motion dataset for France (Traversa et al. 2020) and a weak motion dataset for central and north Europe  
3 (Zaccarelli et al. 2019). We strongly encourage the various ground-motion seismology communities to  
4 collaborate in testing our inferences and in adapting our model to their datasets; especially those not  
5 integrated into ESM.

6 Despite our efforts however, the very high site-response variability at high frequencies remains  
7 a glaring challenge. Site-specific ground-motion prediction using the site-specific random-effects seems  
8 to be the most reasonable approach yet – if we were to avoid the very large ergodic aleatory variability  
9 in seismic hazard and risk assessments. It is however quite encouraging to see several research groups  
10 attempting to investigate and parametrize site-specific characteristics (e.g. shear-wave velocity profiles,  
11 sediment thicknesses, topography, etc)for use in ground-motion models. To aid these efforts and many  
12 other practical applications, we consider ground-motion prediction models in Fourier domain are  
13 extremely useful; especially in quantifying the high frequency ground-motion variabilities.

14 One important aspect we have skipped discussing in this study, for the sake of brevity, is the  
15 analyses of aleatory residuals. These residuals are record-specific and also contain useful information  
16 on secondary phenomena, such as the shear-wave radiation pattern in near-source distances, arrival of  
17 secondary phases at intermediate-far source distances, nonlinear response of soft soils, etc. All these  
18 phenomena can be included into a ground-motion model for more realistic (e.g. anisotropic) predictions.  
19 Of course, to quantify these effects would require much more information (e.g. centroid moment tensor  
20 solutions and incidence angles) in ground-motion datasets. Currently, we are attempting to populate the  
21 ESM dataset with as much of relevant information as possible, in order to facilitate further realism of  
22 ground-motion models. Based on the experience from and utility of this Fourier amplitude ground-  
23 motion model, we plan to pursue such improvements preferably in Fourier domain rather than in  
24 response spectra domain.

25

1  
2  
3  
4  
5  
6  
7

## 8 DATA AND RESOURCES

The European Strong Motion flatfile is available at <https://esm.mi.ingv.it/flatfile-2018/> with persistent identifier PID: 11099/ESM\_flatfile\_2018. The analyses in this study have been performed in R software (Team 2013). In particular, we used the libraries *rlmm* (Koller 2016), *dplyr* (Wickham et al. 2019b), *ggplot2* (Wickham et al. 2019a), *ggmap* (Kahle et al. 2019), *viridis* (Garnier 2019), etc. All the outputs of the robust linear mixed-effects regressions are available for dissemination upon request.

1  
2  
3  
4  
5  
6

## **9 ACKNOWLEDGMENTS**

The contributions of the Sreeram Reddy Kotha (corresponding author) in this research are funded by the SIGMA2 consortium (EDF, CEA, PG&E, SwissNuclear, Orano, CEZ, CRIEPI) under grant – 2017–2021. The model development has benefitted immensely from feedback provided by the collaborators in Horizon 2020 “Seismology and Earthquake Engineering Research Infrastructure Alliance for Europe (SERA)” project.

## 10 REFERENCES

- 1
- 2 Abrahamson NA, Silva WJ, Kamai R (2014) Summary of the ASK14 Ground Motion Relation for  
 3 Active Crustal Regions Earthquake Spectra 30:1025-1055 doi:10.1193/070913eqs198m
- 4 Akkar S et al. (2014) Reference database for seismic ground-motion in Europe (RESORCE) Bulletin  
 5 of earthquake engineering 12:311-339 doi:10.1007/s10518-013-9506-8
- 6 Al Atik L, Abrahamson N, Bommer JJ, Scherbaum F, Cotton F, Kuehn N (2010) The variability of  
 7 ground-motion prediction models and its components Seismological Research Letters  
 8 81:794-801
- 9 Alexis R, Sokos E, Lefils V, Briole P (2021) Seasonal variations in amplitudes and resonance  
 10 frequencies of the HVSR amplification peaks linked to groundwater Geophysical Journal  
 11 International
- 12 Ancheta TD et al. (2014) NGA-West2 database Earthquake Spectra 30:989-1005
- 13 Atik LA, Youngs RR (2014) Epistemic uncertainty for NGA-West2 models Earthquake Spectra  
 14 30:1301-1318
- 15 Bard P-Y, Bora SS, Hollender F, Laurendeau A, Traversa P (2019) Are the Standard V S-Kappa Host-  
 16 to-Target Adjustments the Only Way to Get Consistent Hard-Rock Ground Motion  
 17 Prediction? Pure and Applied Geophysics:1-20
- 18 Basili R et al. (2019) NEAMTHM18 Documentation: the making of the TSUMAPS-NEAM Tsunami  
 19 Hazard Model 2018
- 20 Bayless J, Abrahamson NA (2019a) An Empirical Model for the Interfrequency Correlation of  
 21 Epsilon for Fourier Amplitude Spectra An Empirical Model for the Interfrequency  
 22 Correlation of Epsilon for Fourier Amplitude Spectra Bulletin of the Seismological Society  
 23 of America 109:1058-1070
- 24 Bayless J, Abrahamson NA (2019b) Summary of the BA18 Ground-Motion Model for Fourier  
 25 Amplitude Spectra for Crustal Earthquakes in California Bulletin of the Seismological  
 26 Society of America 109:2088-2105
- 27 Bindi D, Cotton F, Kotha SR, Bosse C, Stromeyer D, Grünthal G (2017a) Application-driven ground  
 28 motion prediction equation for seismic hazard assessments in non-cratonic moderate-  
 29 seismicity areas Journal of Seismology 21:1201-1218 doi:10.1007/s10950-017-9661-5
- 30 Bindi D, Kotha S-R, Weatherill G, Lanzano G, Luzi L, Cotton F (2019a) The pan-European  
 31 engineering strong motion (ESM) flatfile: consistency check via residual analysis Bulletin  
 32 of Earthquake Engineering 17:583-602
- 33 Bindi D, Kotha S (2020) Spectral decomposition of the Engineering Strong Motion (ESM) flat file:  
 34 regional attenuation, source scaling and Arias stress drop Bulletin of Earthquake  
 35 Engineering:1-26
- 36 Bindi D, Parolai S, Grosser H, Milkereit C, Karakisa S (2006) Crustal attenuation characteristics in  
 37 northwestern Turkey in the range from 1 to 10 Hz Bulletin of the Seismological Society of  
 38 America 96:200-214
- 39 Bindi D, Picozzi M, Spallarossa D, Cotton F, Kotha SR (2019b) Impact of Magnitude Selection on  
 40 Aleatory Variability Associated with Ground-Motion Prediction Equations: Part II—  
 41 Analysis of the Between-Event Distribution in Central Italy Bulletin of the Seismological  
 42 Society of America 109:251-262
- 43 Bindi D, Spallarossa D, Pacor F (2017b) Between-event and between-station variability observed  
 44 in the Fourier and response spectra domains: comparison with seismological models  
 45 Geophysical Journal International 210:1092-1104
- 46 Bindi D, Zaccarelli R, Kotha SR (2021) Local and Moment Magnitude Analysis in the Ridgecrest  
 47 Region, California: Impact on Interevent Ground-Motion Variability Bulletin of the  
 48 Seismological Society of America 111:339-355
- 49 Bommer JJ et al. (2015) A SSHAC level 3 probabilistic seismic hazard analysis for a new-build  
 50 nuclear site in South Africa Earthquake Spectra 31:661-698

- 1 Boore DM, Di Alessandro C, Abrahamson NA (2014a) A generalization of the double-corner-  
2 frequency source spectral model and its use in the SCEC BBP validation exercise Bulletin  
3 of the Seismological Society of America 104:2387-2398
- 4 Boore DM, Stewart JP, Seyhan E, Atkinson GM (2014b) NGA-West2 equations for predicting PGA,  
5 PGV, and 5% damped PSA for shallow crustal earthquakes Earthquake Spectra 30:1057-  
6 1085
- 7 Bora SS, Cotton F, Scherbaum F (2019) NGA-West2 Empirical Fourier and Duration Models to  
8 Generate Adjustable Response Spectra Earthquake Spectra 35:61-93  
9 doi:10.1193/110317eqs228m
- 10 Bora SS, Cotton F, Scherbaum F, Edwards B, Traversa P (2017) Stochastic source, path and site  
11 attenuation parameters and associated variabilities for shallow crustal European  
12 earthquakes Bulletin of Earthquake Engineering 15:4531-4561 doi:10.1007/s10518-017-  
13 0167-x
- 14 Bora SS, Scherbaum F, Kuehn N, Stafford P (2014) Fourier spectral-and duration models for the  
15 generation of response spectra adjustable to different source-, propagation-, and site  
16 conditions Bulletin of Earthquake Engineering 12:467-493
- 17 Bora SS, Scherbaum F, Kuehn N, Stafford P (2016) On the relationship between Fourier and  
18 response spectra: Implications for the adjustment of empirical ground-motion prediction  
19 equations (GMPEs) Bulletin of the Seismological Society of America 106:1235-1253
- 20 Brune JN (1970) Tectonic stress and the spectra of seismic shear waves from earthquakes Journal  
21 of geophysical research 75:4997-5009
- 22 Campbell KW, Bozorgnia Y (2014) NGA-West2 Ground Motion Model for the Average Horizontal  
23 Components of PGA, PGV, and 5% Damped Linear Acceleration Response Spectra  
24 Earthquake Spectra 30:1087-1115 doi:10.1193/062913eqs175m
- 25 Chen Y-S, Weatherill G, Pagani M, Cotton F (2018) A transparent and data-driven global tectonic  
26 regionalization model for seismic hazard assessment Geophysical Journal International  
27 213:1263-1280
- 28 Chounet A, Vallée M, Causse M, Courboux F (2018) Global catalog of earthquake rupture  
29 velocities shows anticorrelation between stress drop and rupture velocity Tectonophysics  
30 733:148-158
- 31 Cong L, Mitchell B (1998) Lg coda Q and its relation to the geology and tectonics of the Middle  
32 East. In: Q of the Earth: Global, Regional, and Laboratory Studies. Springer, pp 563-585
- 33 Cotton F, Pousse G, Bonilla F, Scherbaum F (2008) On the discrepancy of recent European ground-  
34 motion observations and predictions from empirical models: Analysis of KiK-net  
35 accelerometric data and point-sources stochastic simulations Bulletin of the Seismological  
36 Society of America 98:2244-2261
- 37 Diaferia G, Cammarano F, Faccenna C (2019) Thermal structure of a vanishing subduction system:  
38 an example of seismically-derived crustal temperature along the Italian peninsula  
39 Geophysical Journal International 219:239-247
- 40 Douglas J (2011) Ground-motion prediction equations 1964-2010. Pacific Earthquake  
41 Engineering Research Center Berkeley, CA,
- 42 Douglas J (2018) Calibrating the backbone approach for the development of earthquake ground  
43 motion models Best Practice in Physics-based Fault Rupture Models for Seismic Hazard  
44 Assessment of Nuclear Installations: Issues and Challenges Towards Full Seismic Risk  
45 Analysis
- 46 Faccioli E, Paolucci R, Vanini M (2015) Evaluation of probabilistic site-specific seismic-hazard  
47 methods and associated uncertainties, with applications in the Po Plain, northern Italy  
48 Bulletin of the Seismological Society of America 105:2787-2807
- 49 Fukushima Y (1996) Scaling relations for strong ground motion prediction models with M 2 terms  
50 Bulletin of the Seismological Society of America 86:329-336
- 51 Garnier S (2019) Viridis: Default color maps from "matplotlib". 2018 URL [https://github](https://github.com/sjmgarnier/viridis)  
52 [com/sjmgarnier/viridis](https://github.com/sjmgarnier/viridis) R package version 03 4:27

- 1 Goulet C et al. Effective amplitude spectrum (EAS) as a metric for ground motion modeling using  
2 Fourier amplitudes. In: 2018 Seismology of the Americas Meeting, 2018.
- 3 Grad M, Tiira T, Group EW (2009) The Moho depth map of the European Plate *Geophysical Journal*  
4 *International* 176:279-292
- 5 Grünthal G, Wahlström R (2012) The European-Mediterranean earthquake catalogue (EMEC) for  
6 the last millennium *Journal of seismology* 16:535-570
- 7 Hollender F, Roumelioti Z, Maufroy E, Traversa P, Mariscal A (2020) Can We Trust High-Frequency  
8 Content in Strong-Motion Database Signals? Impact of Housing, Coupling, and Installation  
9 Depth of Seismic Sensors *Seismological Research Letters* 91:2192-2205
- 10 Holmgren JM, Atkinson GM (2018) Effect of Uncertainty in Source Parameters on Ground-Motion  
11 Variability for Potentially Induced Earthquakes in the Central United States *Seismological*  
12 *Research Letters* 89:702-711 doi:10.1785/0220170208
- 13 Jacoby WG (2000) Loess:: a nonparametric, graphical tool for depicting relationships between  
14 variables *Electoral Studies* 19:577-613
- 15 Jarvis A, Reuter H, Nelson A, Guevara E (2008) Hole-Filled Seamless SRTM Data V4: International  
16 Centre for Tropical Agriculture (CIAT): <http://srtm.csi.cgiar.org>, accessed 31
- 17 Kahle D, Wickham H, Kahle MD (2019) Package ‘ggmap’
- 18 Kohrangi M, Kotha SR, Bazzurro P (2020) Impact of Partially Non-Ergodic Site-specific  
19 Probabilistic Seismic Hazard on Risk Assessment of Single Buildings Earthquake spectra  
20 (in-review)
- 21 Koller M (2016) *robustlmm*: An R package for robust estimation of linear mixed-effects models  
22 *Journal of statistical software* 75:1-24
- 23 Kotha SR, Bindi D, Cotton F (2016) Partially non-ergodic region specific GMPE for Europe and  
24 Middle-East *Bulletin of Earthquake Engineering* 14:1245-1263
- 25 Kotha SR, Bindi D, Cotton F (2017) From ergodic to region- and site-specific probabilistic seismic  
26 hazard assessment: Method development and application at European and Middle Eastern  
27 sites *Earthquake spectra* 33:1433-1453 doi:10.1193/081016EQS130M
- 28 Kotha SR, Cotton F, Bindi D (2018) A new approach to site classification: Mixed-effects Ground  
29 Motion Prediction Equation with spectral clustering of site amplification functions *Soil*  
30 *Dynamics and Earthquake Engineering* doi:10.1016/j.soildyn.2018.01.051
- 31 Kotha SR, Cotton F, Bindi D (2019) Empirical models of shear-wave radiation pattern derived from  
32 large datasets of ground-shaking observations *Scientific reports* 9
- 33 Kotha SR, Weatherill G, Bindi D, Cotton F (2020) A Regionally Adaptable Ground-Motion Model  
34 for Shallow Crustal Earthquakes in Europe *Bulletin of Earthquake Engineering* 18:4091-  
35 4125 doi: 10.1007/s10518-020-00869-1
- 36 Kowsari M, Halldorsson B, Hrafnkelsson B, Snæbjörnsson JP, Jónsson S (2019) Calibration of  
37 ground motion models to Icelandic peak ground acceleration data using Bayesian Markov  
38 Chain Monte Carlo simulation *Bulletin of Earthquake Engineering* 17:2841-2870
- 39 Kuehn NM, Abrahamson NA (2017) The Effect of Uncertainty in Predictor Variables on the  
40 Estimation of Ground-Motion Prediction Equations *Bulletin of the Seismological Society*  
41 *of America* 108:358-370 doi:10.1785/0120170166
- 42 Lanzano G et al. (2018) The pan-European engineering strong motion (ESM) flatfile: compilation  
43 criteria and data statistics *Bulletin of Earthquake Engineering*:1-22
- 44 Loviknes K, kotha SR, Cotton F, Schorlemmer D (2021) Testing ground-motion models non-linear  
45 amplification factors *Bulletin of Seismological Society of America*
- 46 Lu Y, Stehly L, Paul A, Group AW (2018) High-resolution surface wave tomography of the  
47 European crust and uppermost mantle from ambient seismic noise *Geophysical Journal*  
48 *International* 214:1136-1150
- 49 Mayor J, Traversa P, Calvet M, Margerin L (2018) Tomography of crustal seismic attenuation in  
50 Metropolitan France: implications for seismicity analysis *Bulletin of Earthquake*  
51 *Engineering* 16:2195-2210

- 1 Mitchell BJ, Cong L, Ekström G (2008) A continent-wide map of 1-Hz Lg coda Q variation across  
 2 Eurasia and its relation to lithospheric evolution *Journal of Geophysical Research: Solid*  
 3 *Earth* 113
- 4 Mucciarelli M, Gallipoli MR, Lizza C, Vignola L (2017) Site condition at accelerometric stations in  
 5 Southern Italy: observations gained from peculiar cases *Bulletin of Earthquake*  
 6 *Engineering* 15:2367-2376
- 7 Péquegnat C, Guéguen P, Hatzfeld D, Langlais M (2008) The French accelerometric network (RAP)  
 8 and national data centre (RAP-NDC) *Seismological Research Letters* 79:79-89
- 9 Perrin C, Manighetti I, Ampuero JP, Cappa F, Gaudemer Y (2016) Location of largest earthquake  
 10 slip and fast rupture controlled by along-strike change in fault structural maturity due to  
 11 fault growth *Journal of Geophysical Research: Solid Earth* 121:3666-3685
- 12 Pilz M, Cotton F (2019) Does the One-Dimensional Assumption Hold for Site Response Analysis?  
 13 A Study of Seismic Site Responses and Implication for Ground Motion Assessment Using  
 14 KiK-Net Strong-Motion Data *Earthquake Spectra* 35:883-905
- 15 Pilz M, Cotton F, Zaccarelli R, Bindi D (2019) Capturing Regional Variations of Hard-Rock  
 16 Attenuation in Europe *Bulletin of the Seismological Society of America*
- 17 Radiguet M, Cotton F, Manighetti I, Campillo M, Douglas J (2009) Dependency of near-field ground  
 18 motions on the structural maturity of the ruptured faults *Bulletin of the Seismological*  
 19 *Society of America* 99:2572-2581
- 20 Ritsema J, Deuss aA, Van Heijst H, Woodhouse J (2011) S40RTS: a degree-40 shear-velocity model  
 21 for the mantle from new Rayleigh wave dispersion, teleseismic traveltimes and normal-  
 22 mode splitting function measurements *Geophysical Journal International* 184:1223-1236
- 23 Rodriguez-Marek A et al. (2013) A model for single-station standard deviation using data from  
 24 various tectonic regions *Bulletin of the seismological society of America* 103:3149-3163
- 25 Roumelioti Z, Hollender F, Guéguen P (2020) Rainfall-Induced Variation of Seismic Waves Velocity  
 26 in Soil and Implications for Soil Response: What the ARGONET (Cephalonia, Greece)  
 27 Vertical Array Data Reveal *Bulletin of the Seismological Society of America* 110:441-451
- 28 Sahakian V, Baltay A, Hanks T, Buehler J, Vernon F, Kilb D, Abrahamson N (2019) Ground-Motion  
 29 Residuals, Path Effects, and Crustal Properties: A Pilot Study in Southern California *Journal*  
 30 *of Geophysical Research: Solid Earth*
- 31 Stafford PJ (2017) Interfrequency Correlations among Fourier Spectral Ordinates and  
 32 Implications for Stochastic Ground-Motion Simulation *Interfrequency Correlations among*  
 33 *Fourier Spectral Ordinates and Implications* *Bulletin of the Seismological Society of*  
 34 *America* 107:2774-2791
- 35 Stewart JP (2000) Variations between foundation-level and free-field earthquake ground motions  
 36 *Earthquake Spectra* 16:511-532
- 37 Team RC (2013) R foundation for statistical computing Vienna, Austria 3
- 38 Traversa P et al. (2020) RESIF RAP and RLBP dataset of earthquake ground motion in mainland  
 39 France *Seismological Research Letters*
- 40 Venables W, Ripley B (2002) *Modern applied statistics* (Fourth S., editor) New York. Springer,
- 41 Weatherill G, Crowley H, Lemoine A, Roullé A, Tourlière B, Kotha SR, Cotton F (2020a) Modelling  
 42 Seismic Site Response at Regional Scale for the 2020 European Seismic Risk Model  
 43 (ESRM20) *Bulletin of Earthquake Engineering in-preparation*
- 44 Weatherill G, Kotha SR, Cotton F (2020b) Re-thinking Site Amplification in Regional Seismic Risk  
 45 Assessment *Earthquake spectra* doi:10.1177/8755293019899956
- 46 Weatherill G, Kotha SR, Cotton F (2020c) A Regionally-Adaptable "Scaled-Backbone" Ground  
 47 Motion Logic Tree for Shallow Seismicity in Europe: Application in the 2020 European  
 48 Seismic Hazard Model *Bulletin of Earthquake Engineering*
- 49 Weatherill G, Kotha SR, Cotton F, Bindi D, Danciu L (2020d) Updated GMPE logic tree and rock/soil  
 50 parameterisation for ESHM18 vol Deliverable 25.4. *Seismology and Earthquake*  
 51 *Engineering Research Infrastructure Alliance for Europe (SERA)*,

- 1 Weatherill G, Pagani M, Garcia J (2016) Exploring earthquake databases for the creation of  
2 magnitude-homogeneous catalogues: tools for application on a regional and global scale  
3 Geophysical Journal International 206:1652-1676  
4 Wickham H, Chang W, Henry L, Pedersen T, Takahashi K, Wilke C, Woo K (2019a) R Package  
5 'ggplot2'v. 3.1. 1 Cran R  
6 Wickham H, François R, Henry L, Müller K (2019b) dplyr: A Grammar of Data Manipulation. R  
7 package version 0.8. 0.1. ed,  
8 Youngs R, Abrahamson N, Makdisi F, Sadigh K (1995) Magnitude-dependent variance of peak  
9 ground acceleration Bulletin of the Seismological Society of America 85:1161-1176  
10 Zaccarelli R, Bindi D, Strollo A, Quinteros J, Cotton F (2019) Stream2segment: An Open-Source  
11 Tool for Downloading, Processing, and Visualizing Massive Event-Based Seismic  
12 Waveform Datasets Seismological Research Letters 90:2028-2038  
13 Zhu C, Weatherill G, Cotton F, Pilz M, Kwak DY, Kawase H (2020) An Open-Source Site Database of  
14 Strong-Motion Stations in Japan: K-NET and KiK-net  
15

# Figures

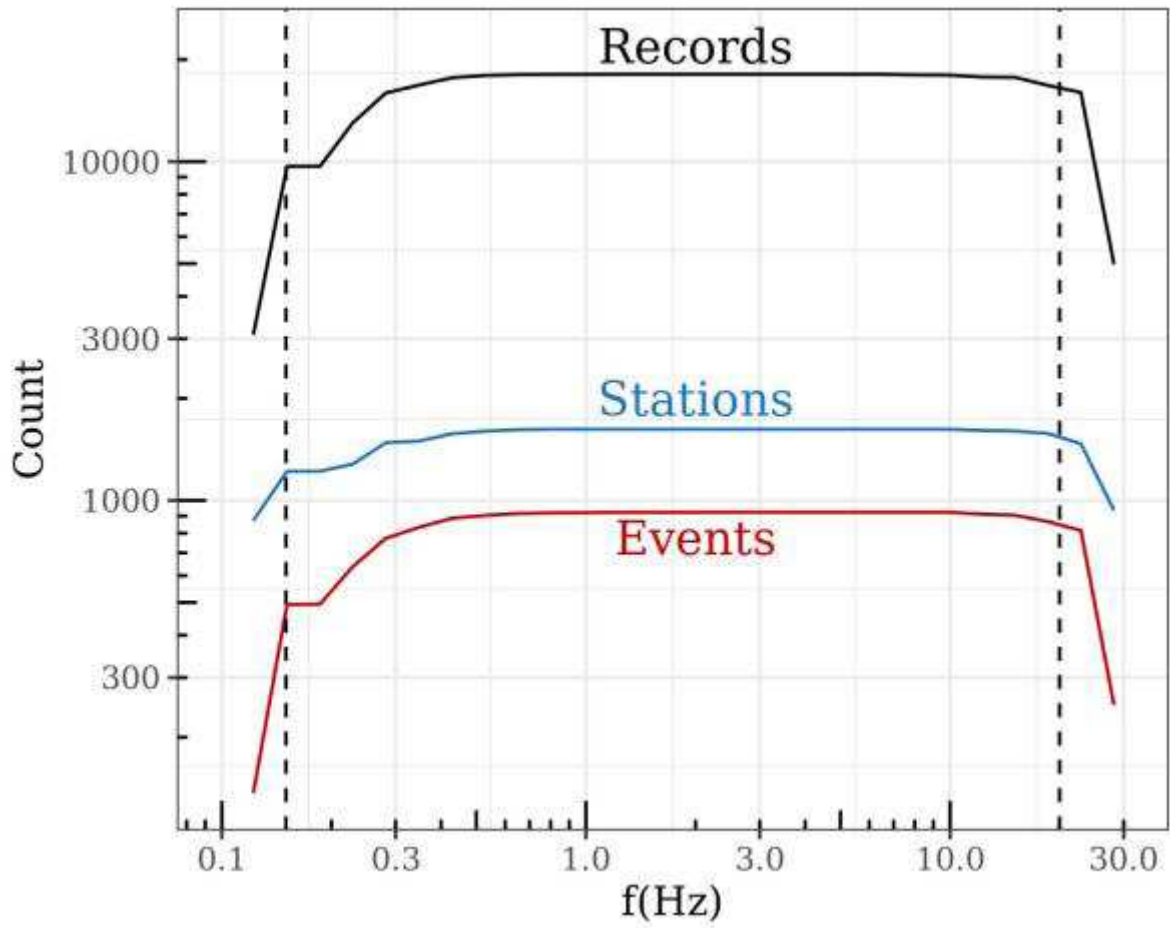
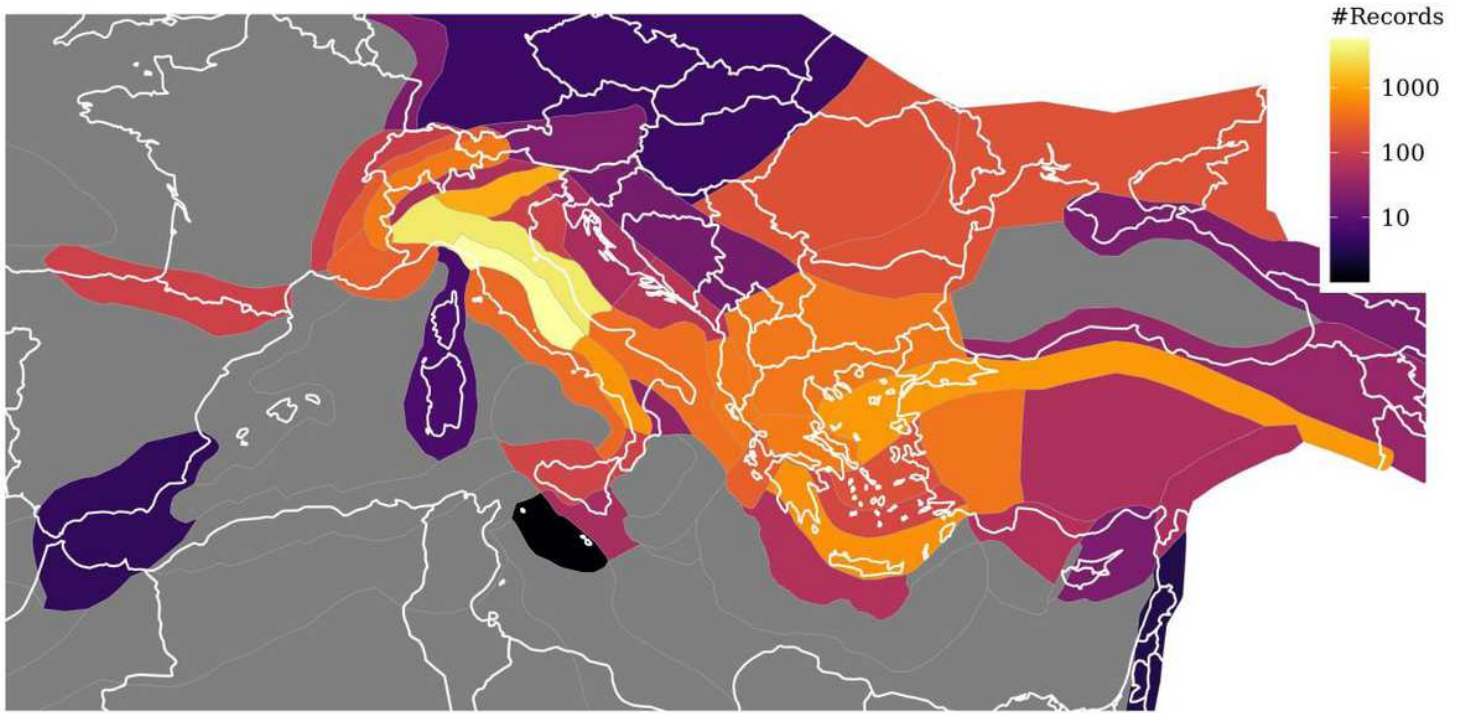


Figure 1

Number of records, events, and stations used in regression at each frequency



**Figure 2**

Distribution of records in each of the 45 attenuation regionalisation polygons Note: The designations employed and the presentation of the material on this map do not imply the expression of any opinion whatsoever on the part of Research Square concerning the legal status of any country, territory, city or area or of its authorities, or concerning the delimitation of its frontiers or boundaries. This map has been provided by the authors.

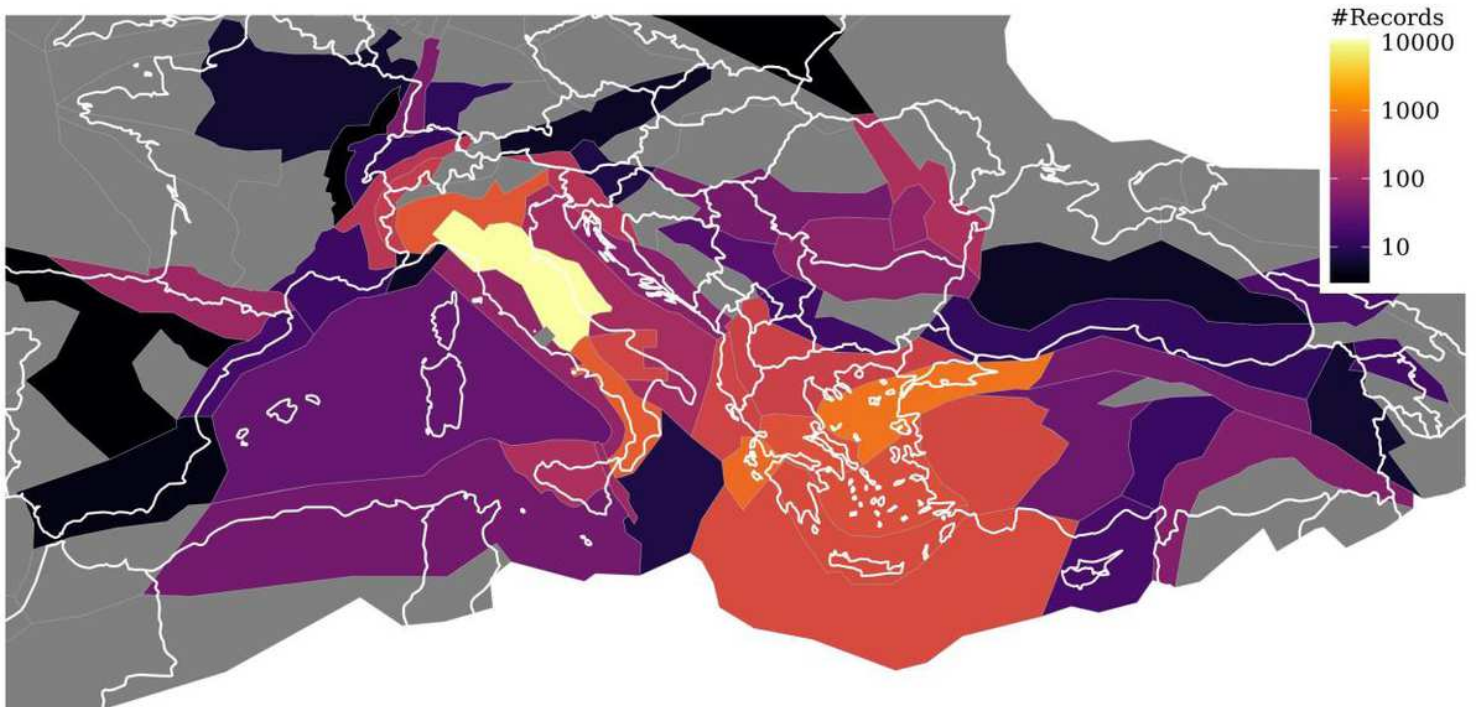


**Figure 3**

Distribution of records from shallow crustal events in each of the 55 event localisation polygons (tectonic zones) Note: The designations employed and the presentation of the material on this map do not imply the expression of any opinion whatsoever on the part of Research Square concerning the legal status of any country, territory, city or area or of its authorities, or concerning the delimitation of its frontiers or boundaries. This map has been provided by the authors.

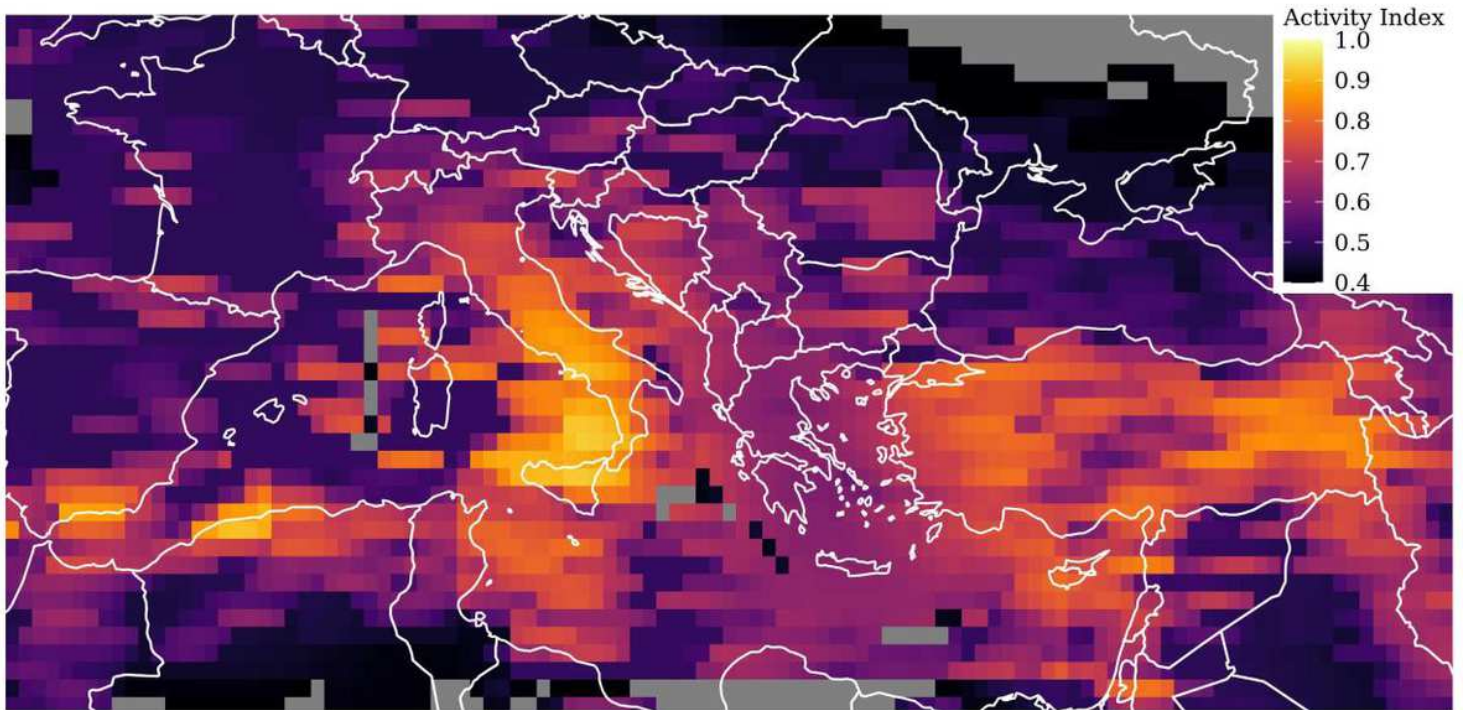


**Figure 4**

Activity Index map of pan-European region by Chen et al. (2018) Note: The designations employed and the presentation of the material on this map do not imply the expression of any opinion whatsoever on the part of Research Square concerning the legal status of any country, territory, city or area or of its authorities, or concerning the delimitation of its frontiers or boundaries. This map has been provided by the authors.

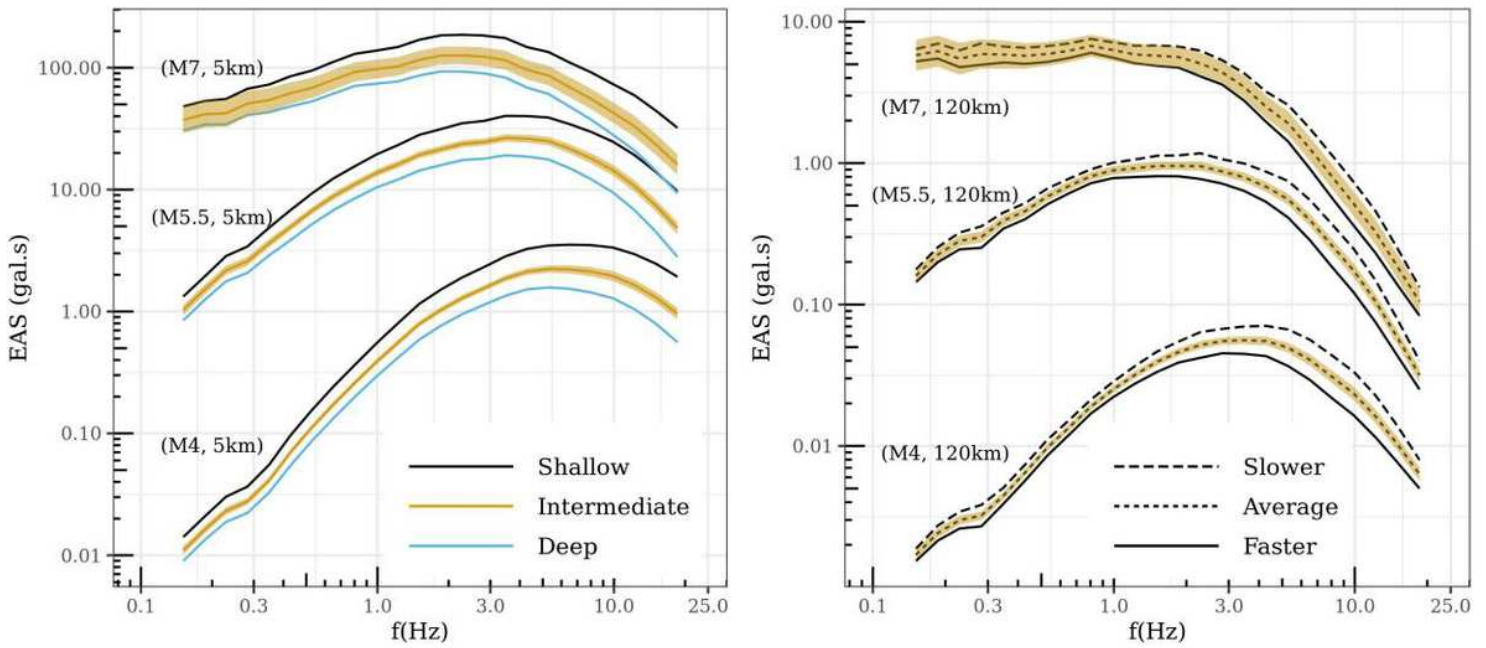


**Figure 5**

Predicted Fourier spectra of the GMM-FA for various scenarios, differentiated by color for Shallow ( $\leq 10$ ), Intermediate ( $10 \leq \leq 20$ ), and Deep ( $20 \leq$ ) events in the left panel. In the right panel are the Fourier spectra differentiated by regional anelastic attenuation: Slower and Faster than pan-European Average

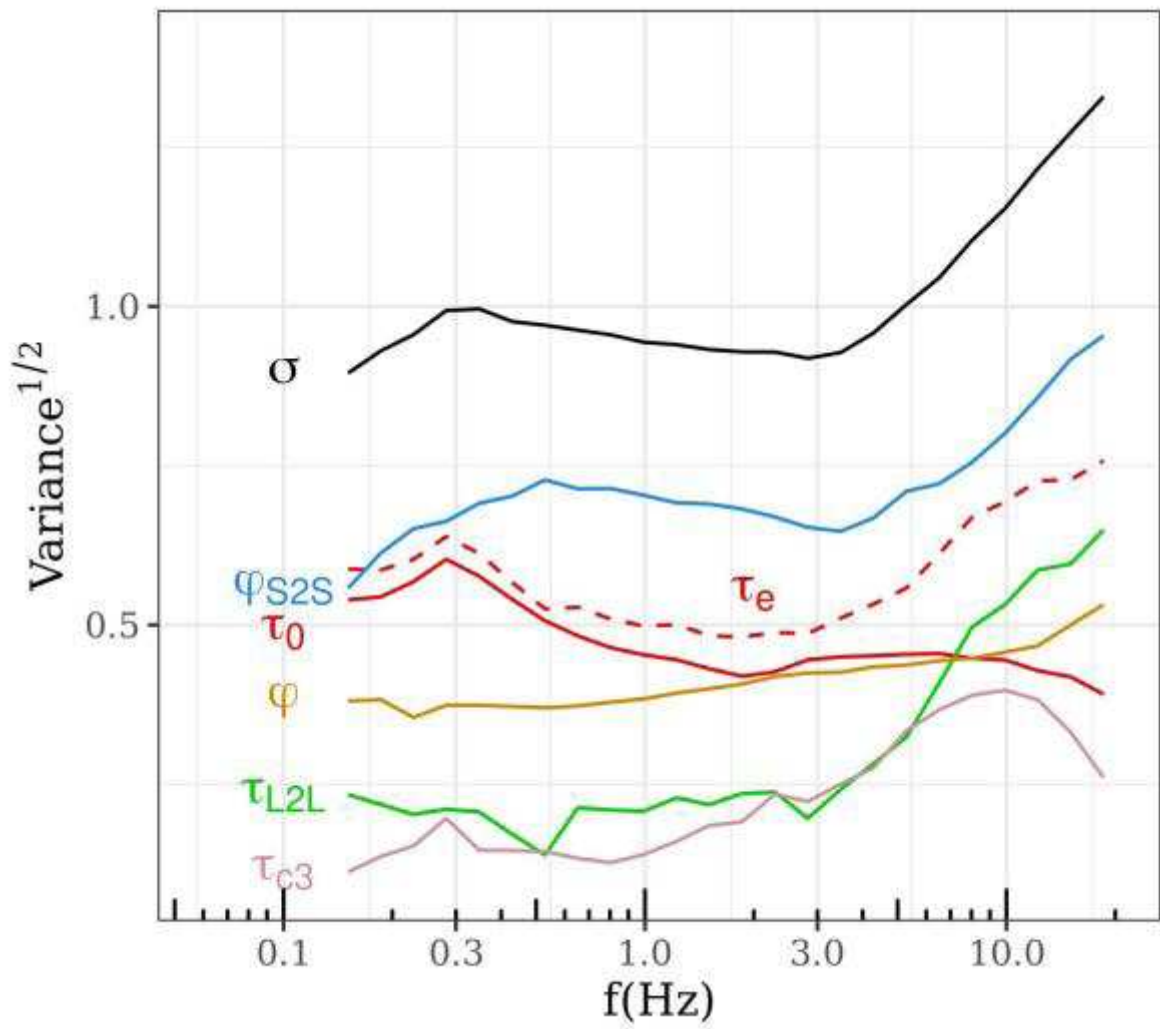
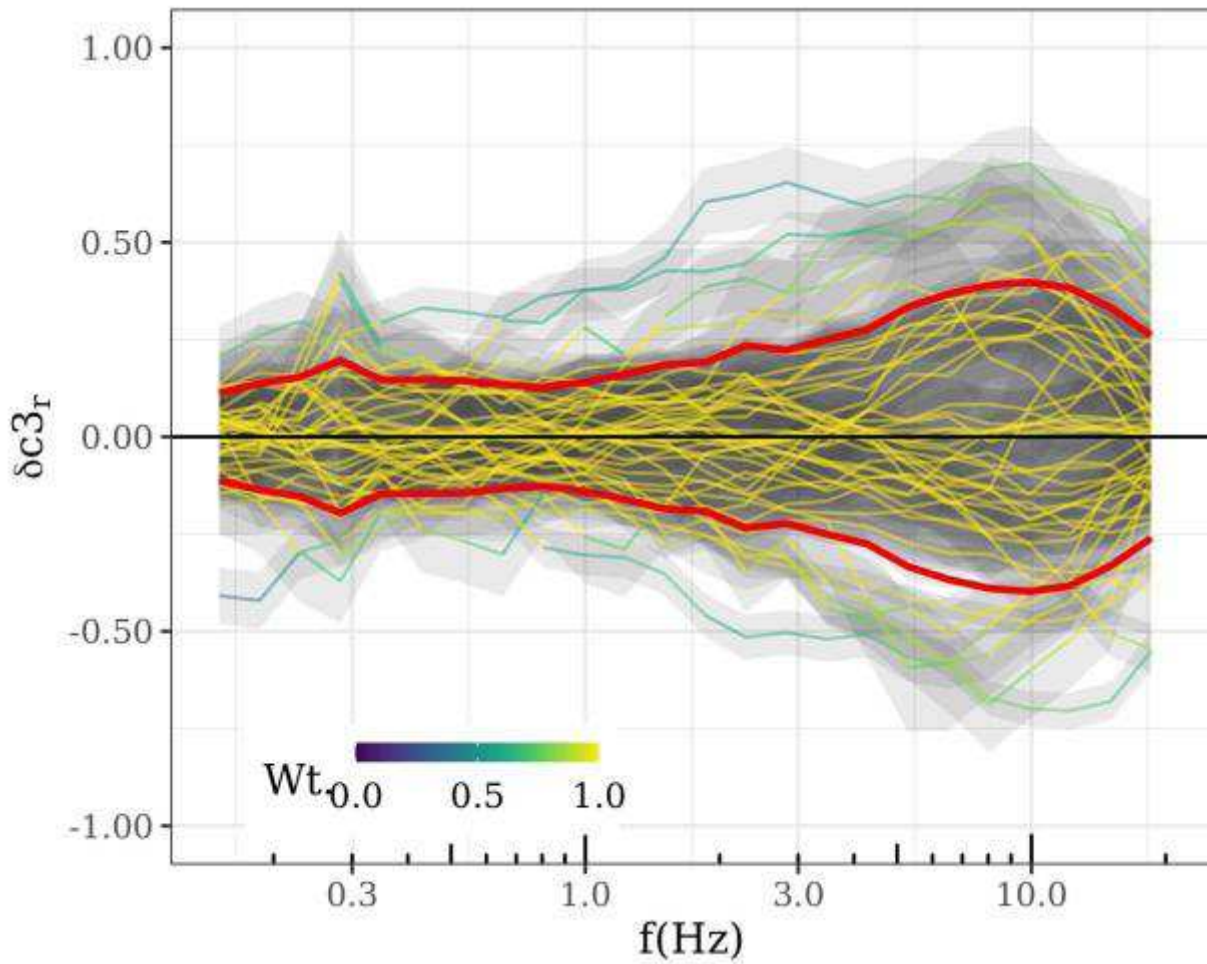


Figure 6

Please see the Manuscript PDF file for the complete figure caption.



**Figure 7**

$\delta C_3$ , for  $\lambda = 0.15-20$ . Each line corresponds to one of the 45 attenuation regions, with colors indicating their weight in robust regression. Overlain red curves mark the  $\pm 1.345$  values. Regions with  $\delta C_3(\lambda)$  beyond  $\pm 1.345$  are given a lower than a unit weight

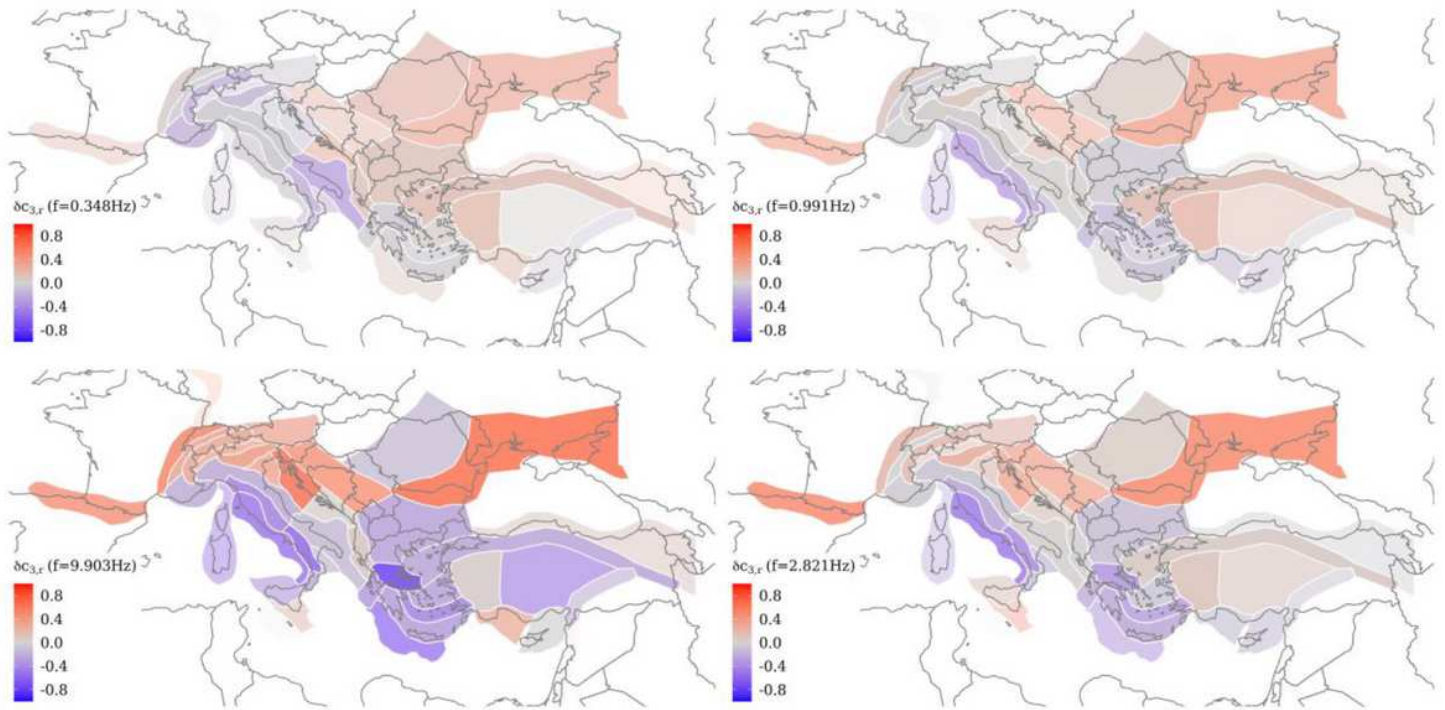


**Figure 8**

$\delta c_{3,r}$  variation across the 45 regions in ESM dataset for  $f=0.3, 1, 3, 10$  (clockwise from top-left to bottom-left panels). Blue polygons locate regions with anelastic attenuation faster than the pan-European average, red polygons locate regions with slower attenuation, and grey polygons are regions close to the average. Regions with fewer ground-motion observations, thereby larger epistemic error on  $\delta c_{3,r}$ , are more transparent and appear fainter. Note that the color scale is the same in all the maps in order to emphasize the frequency dependence of spatial variability of anelastic attenuation. Note: The designations employed and the presentation of the material on this map do not imply the expression of any opinion whatsoever on the part of Research Square concerning the legal status of any country, territory, city or area or of its authorities, or concerning the delimitation of its frontiers or boundaries. This map has been provided by the authors.

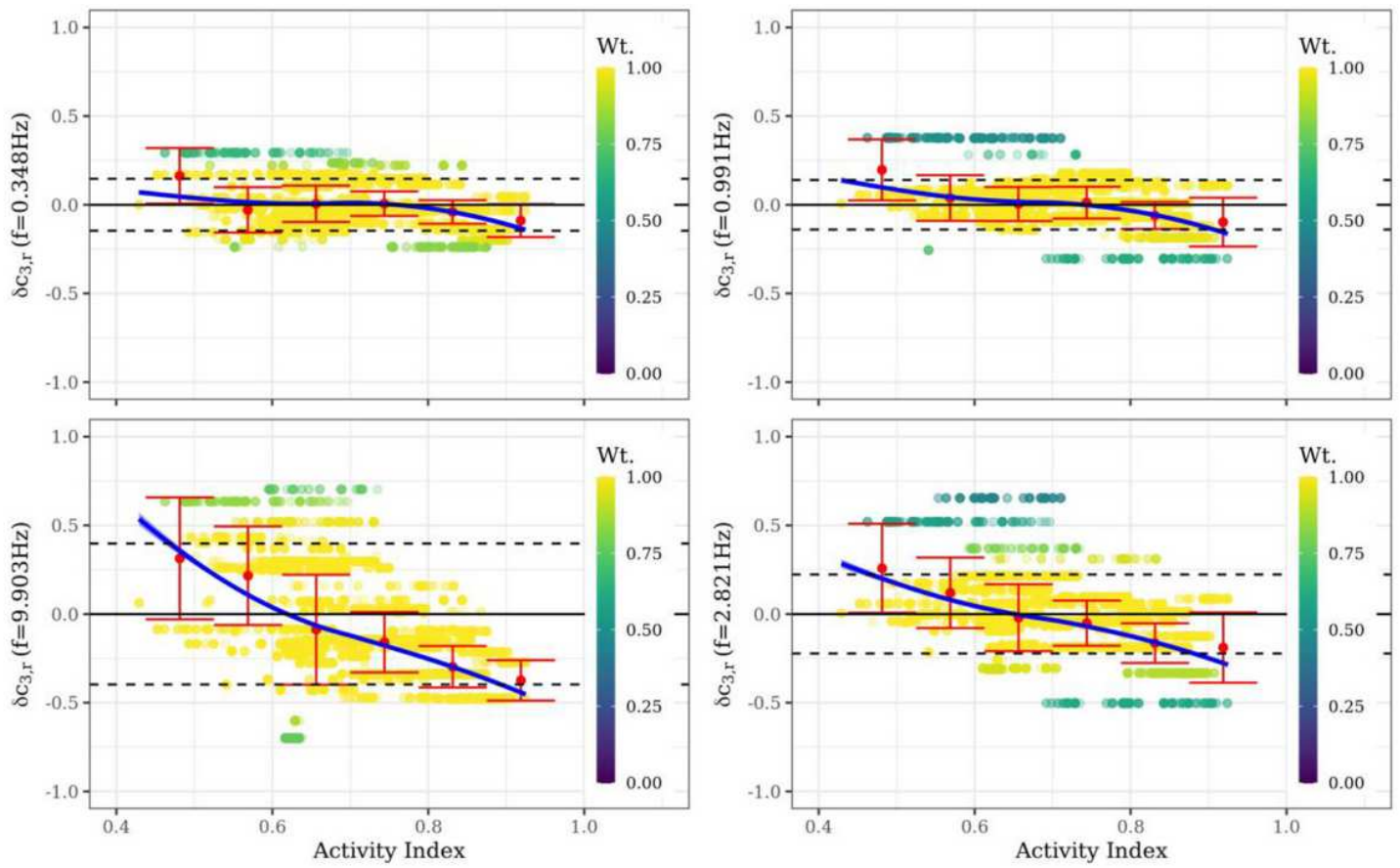


**Figure 9**

$\delta c_{3,r}$  of the 45 regions versus Activity Index at site locations within each region, for  $f \approx 0.3, 1, 3, 10$  (clockwise from top-left to bottom-left). The blue lines are loess fits between the two parameters. Marker colors indicate the weight assigned to  $\delta c_{3,r}$  of each region in the rlmm regression

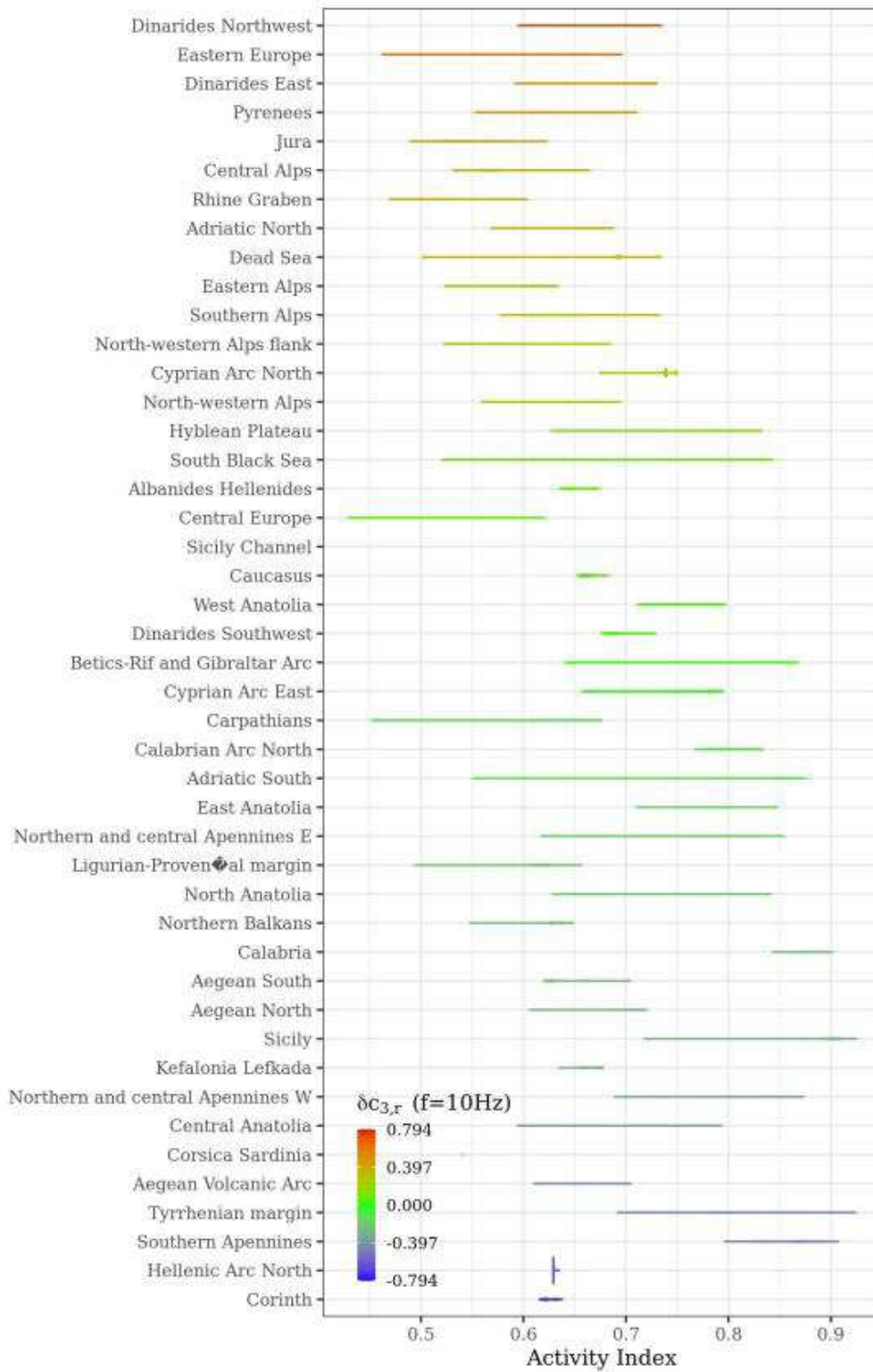
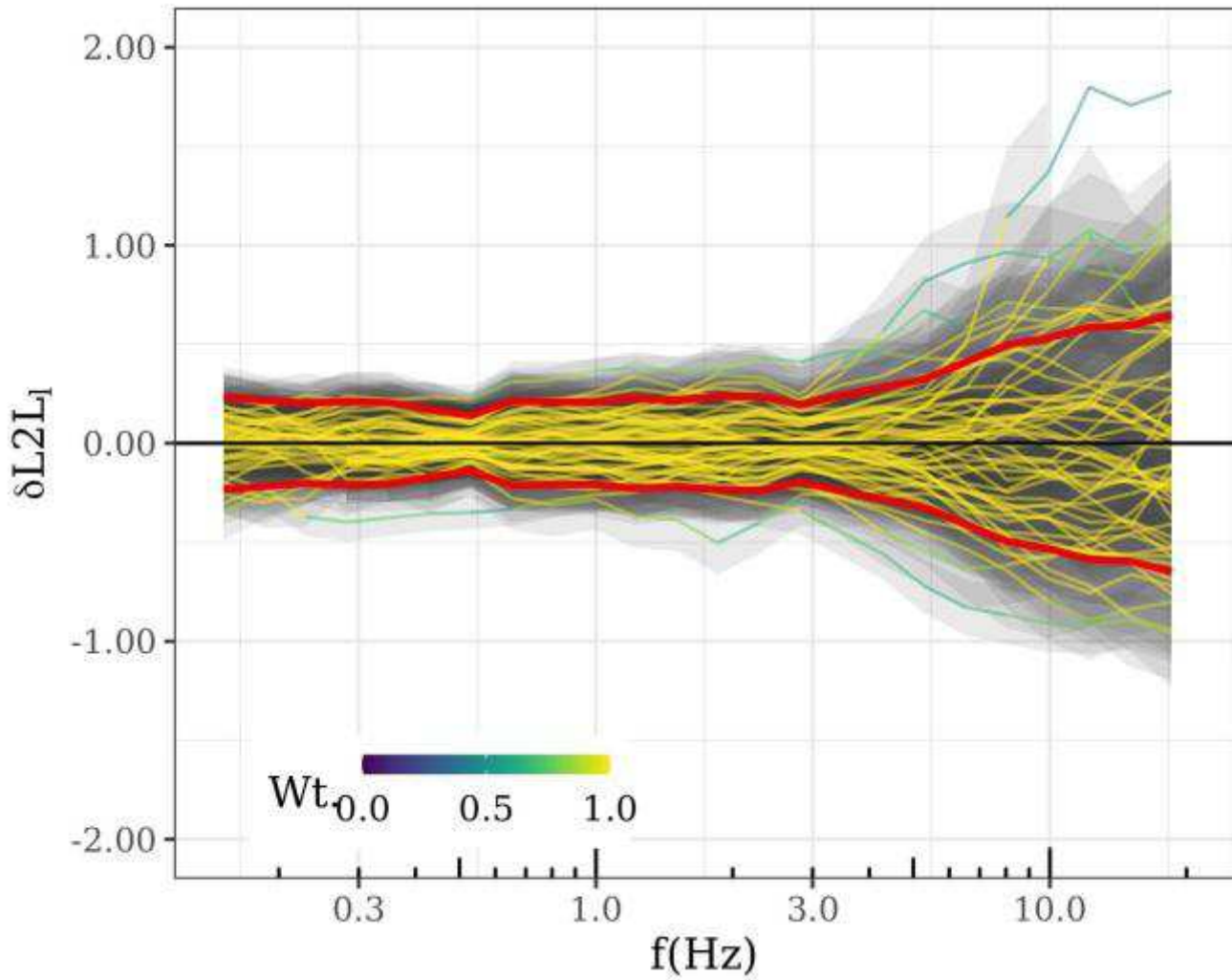


Figure 10

$\Delta C_{3,r}$  at  $f \approx 10\text{Hz}$  of the 45 regions versus the range of Activity Index at site locations within each region



**Figure 11**

$\Delta L_2 L_1$  for  $f = 0.15-20$  Hz. Each line corresponds to one of the 55 tectonic localities, with colors indicating their weight in rlm regression. Overlain red curves mark the  $\pm 1.345\sigma$  values. Localities with  $\Delta L_2 L_1(f)$  beyond  $\pm 1.345\sigma$  are given a weight lower than one

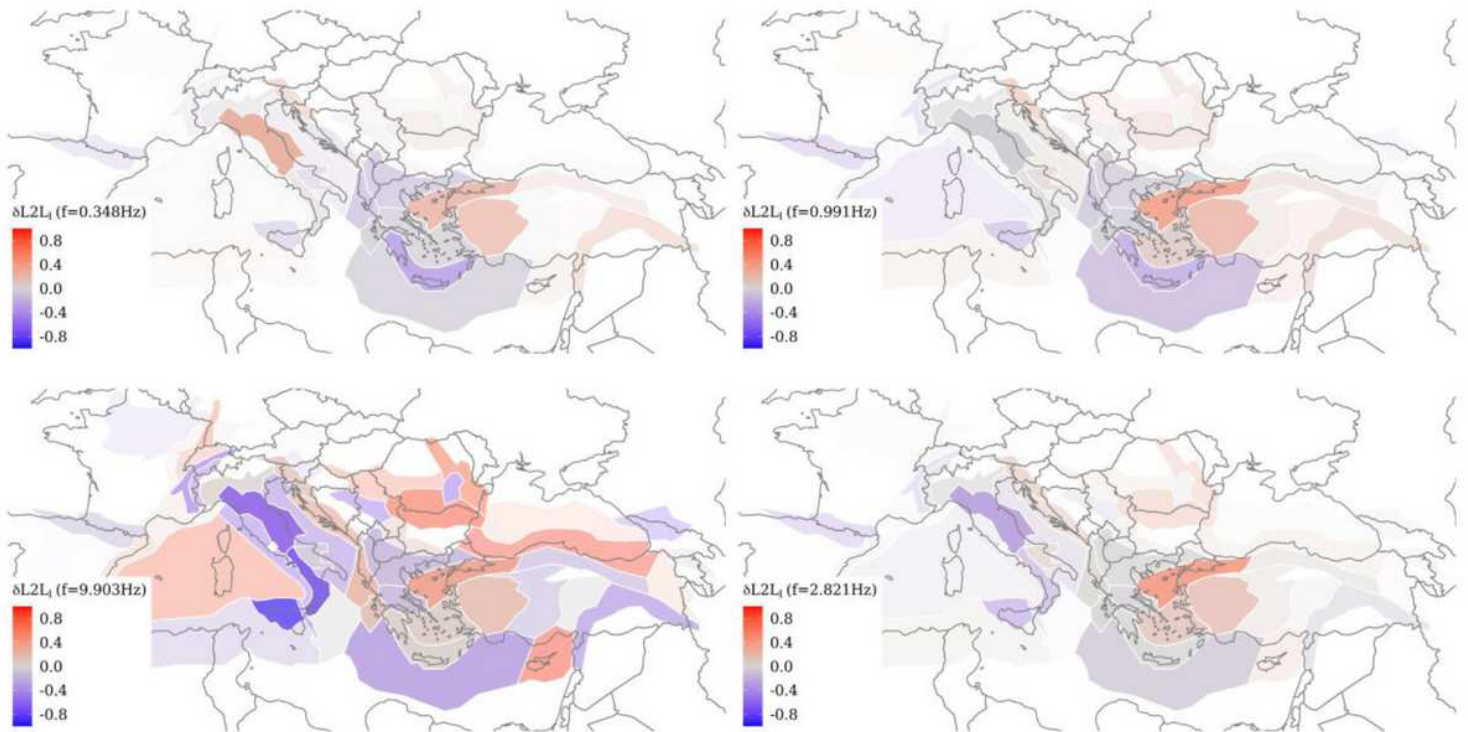


**Figure 12**

Tectonic localities and the  $\delta L2L1$  for these locality polygons. Red colored localities produced events capable of higher  $\delta L2L1$  ( $\delta = 0.3, 1, 3, 10$ ) than the GMM median predictions, blue colored localities produced earthquakes weaker than dataset average, and grey colored localities are close to the dataset average. Localities with fewer ground-motion observations, thereby larger epistemic error on  $\delta L2L1$ , are more transparent and appear fainter. Note that the color scale is the same in all the maps in order to emphasize the frequency dependence of spatial variability of event characteristics. Note: The designations employed and the presentation of the material on this map do not imply the expression of any opinion whatsoever on the part of Research Square concerning the legal status of any country, territory, city or area or of its authorities, or concerning the delimitation of its frontiers or boundaries. This map has been provided by the authors.

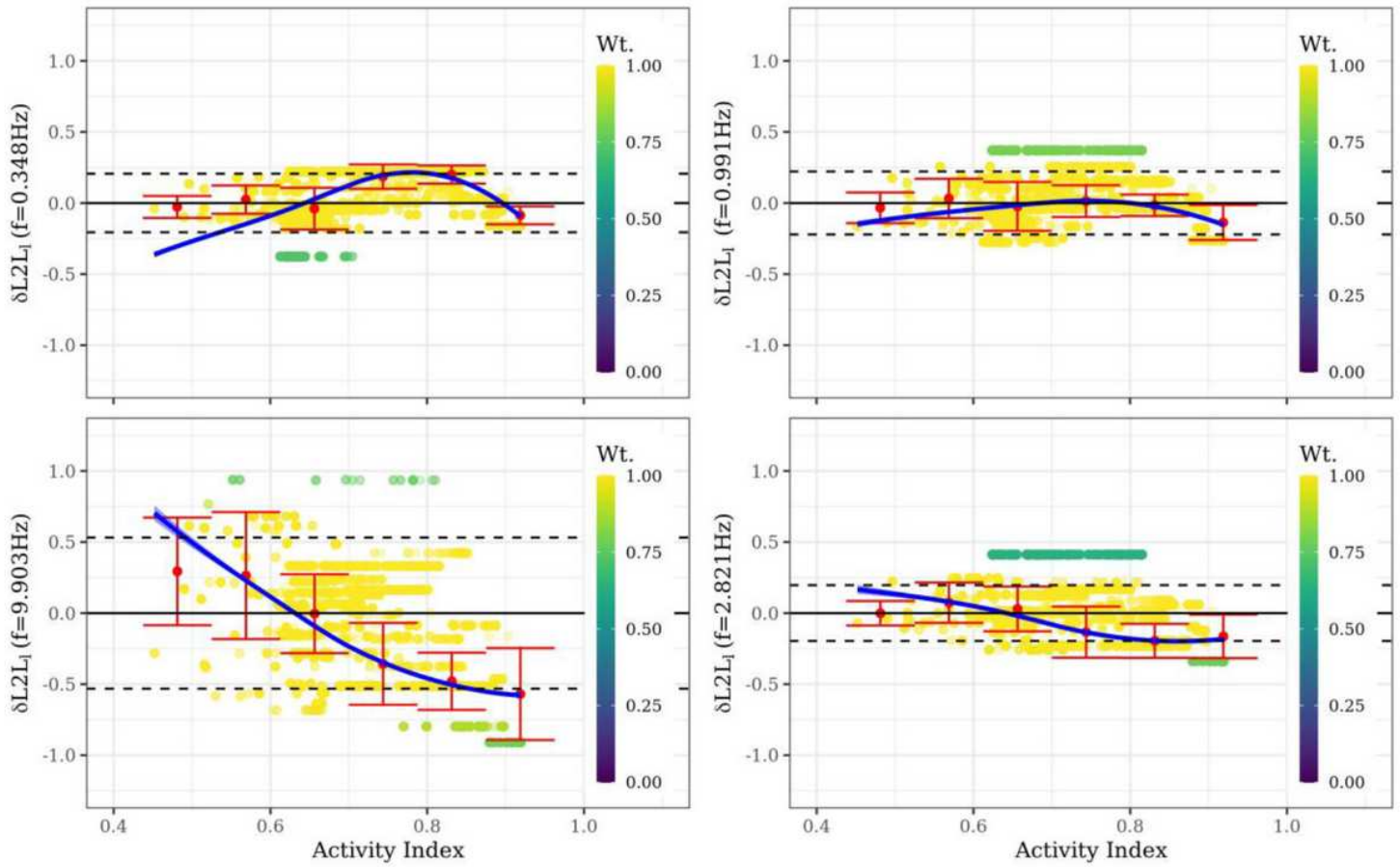


**Figure 13**

Activity Index of the 55 tectonic localities versus  $\delta L2L_1$  at event locations within each locality, for  $f=0.3, 1, 3, 10$  Hz (clockwise from top-left to bottom-left). The blue lines are loess fits between the two parameters. Marker colors indicate the weight assigned to  $\delta L2L_1$  of each locality in the rlm regression

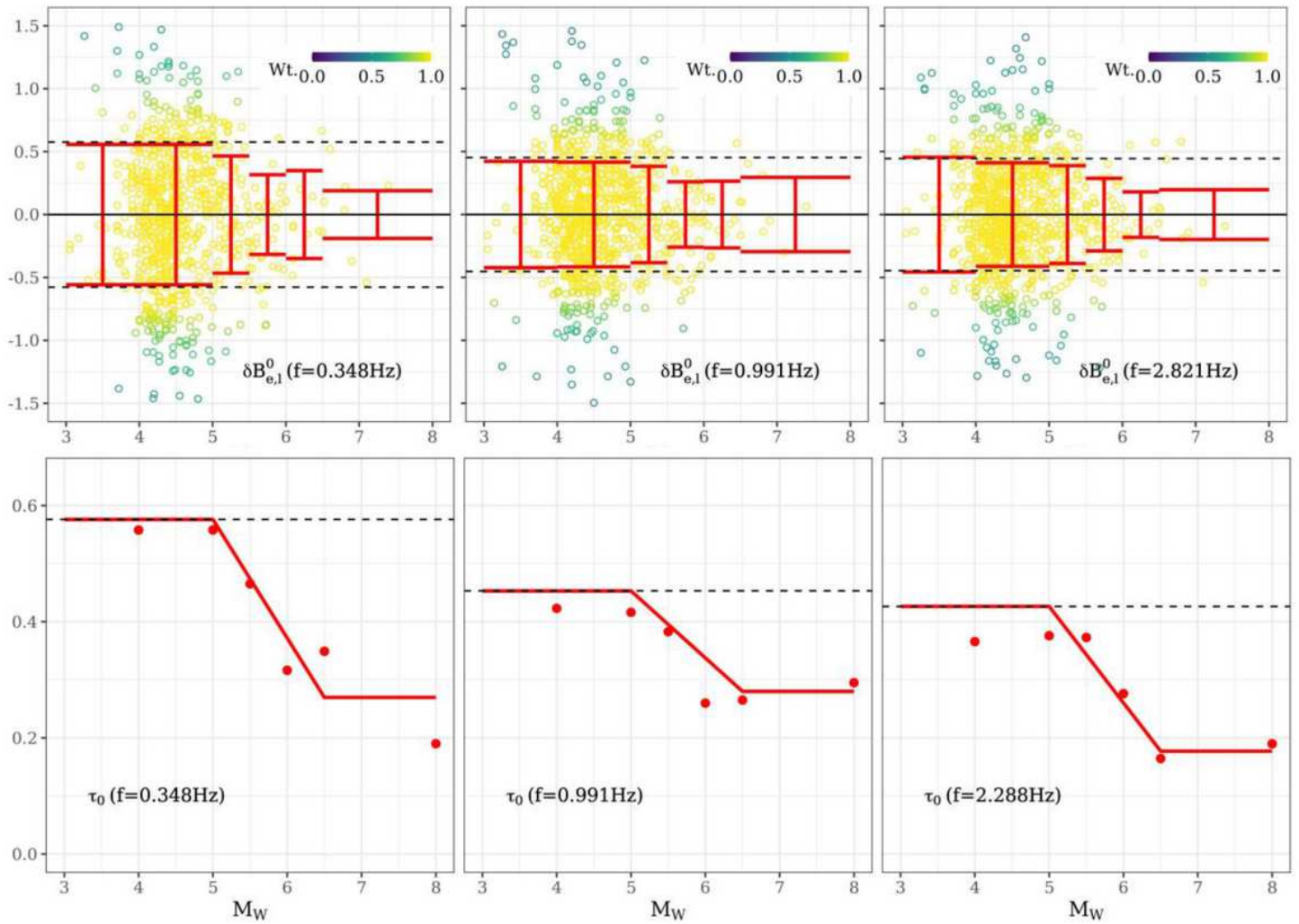


**Figure 14**

Magnitude and frequency dependent heteroskedasticity of between-event variability  $\tau_0$ . Top row panels show  $\delta B_{e,1}^0 \sim \tau_0$  at  $f \approx 0.3, 1, 3\text{Hz}$ , wherein the marker colors are  $Wt$  weights, black dotted lines delimit  $\pm 0.5$ , and red error bars indicate the Median Absolute Deviation (MAD) in bins (details in main text). Bottom row panels show the fitted magnitude dependent  $\tau_0$  in red against the black dashed line of homoskedastic  $\tau_0$ .

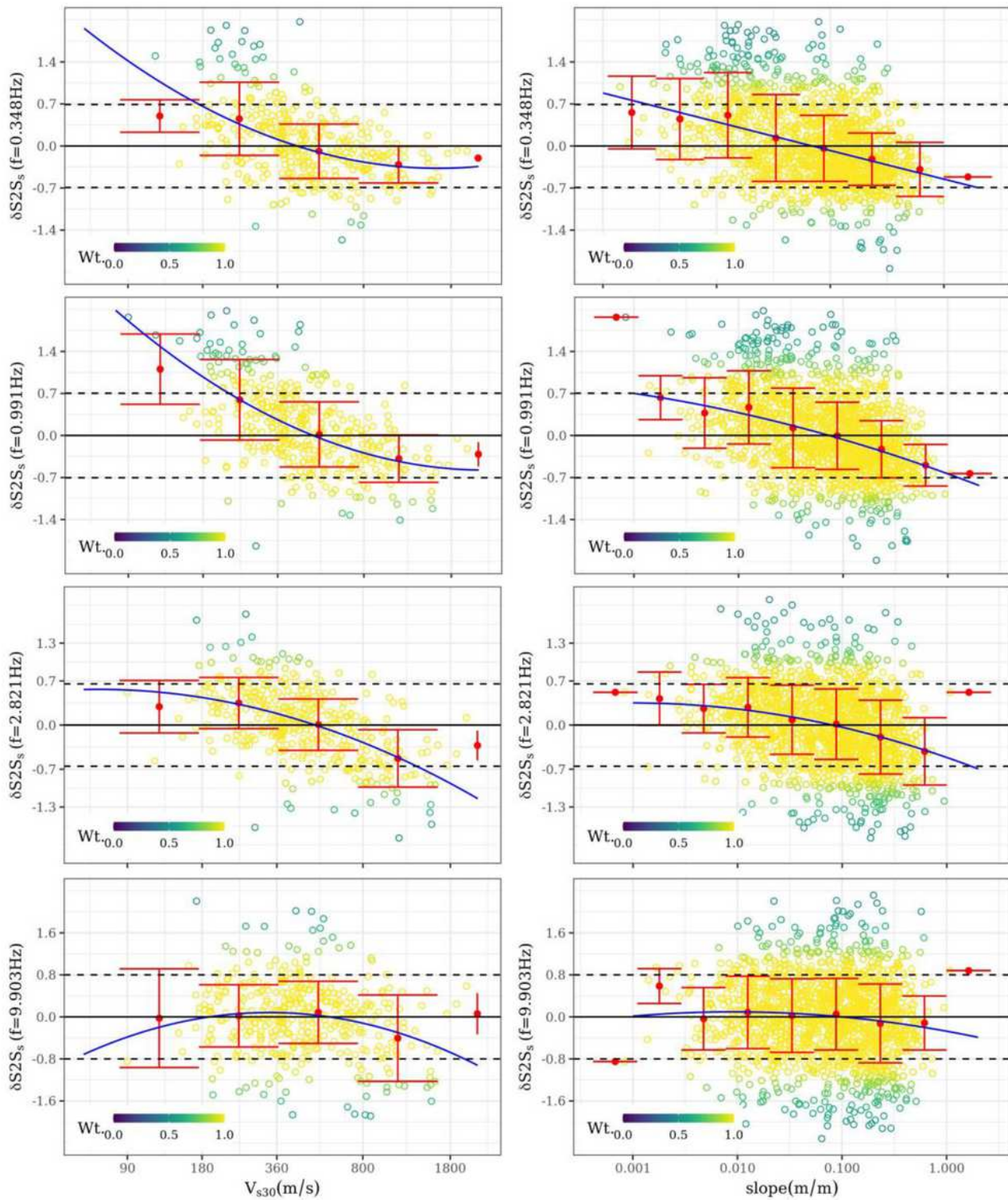


**Figure 15**

Plot showing the trend of  $\delta S2S_s$  ( $f \approx 0.3, 1, 3, 10$ ) (from top to bottom rows) with  $V_{s30}$  (left column) and topographic slope at site location (right column). Note that only 400 sites have measured  $V_{s30}$  in the ESM dataset, while all 1622 sites have topographic slope values.

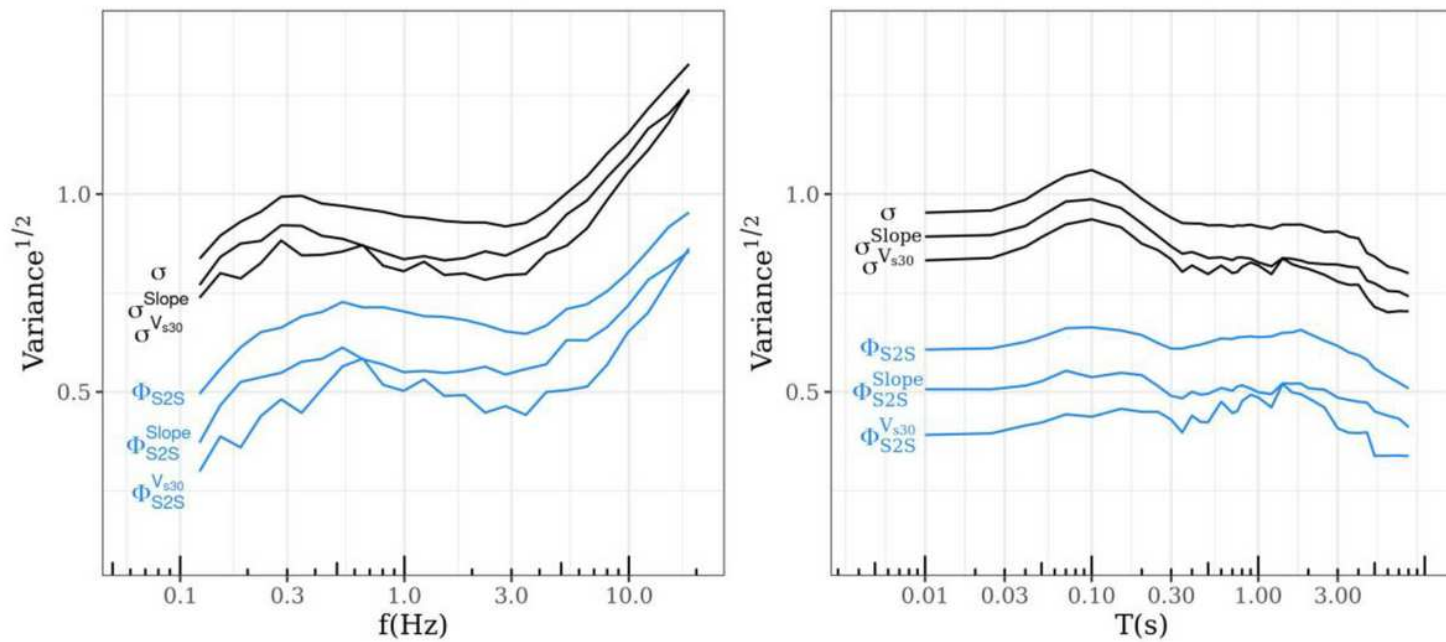


Figure 16

Please see the Manuscript PDF file for the complete figure caption.

## Supplementary Files

This is a list of supplementary files associated with this preprint. Click to download.

- [Supplementaryfigures.pdf](#)